

See discussions, stats, and author profiles for this publication at: <http://www.researchgate.net/publication/280643324>

Hippocampal circuit dysfunction in the Tc1 mouse model of Down syndrome

ARTICLE *in* NATURE NEUROSCIENCE · AUGUST 2015

Impact Factor: 14.98 · DOI: 10.1038/nn.4072

DOWNLOADS

19

VIEWS

30

18 AUTHORS, INCLUDING:



[Jonathan Witton](#)

University of Bristol

7 PUBLICATIONS 94 CITATIONS

[SEE PROFILE](#)



[Damian M. Cummings](#)

University College London

29 PUBLICATIONS 732 CITATIONS

[SEE PROFILE](#)



[Frances A Edwards](#)

University College London

56 PUBLICATIONS 3,529 CITATIONS

[SEE PROFILE](#)



[Michael G Stewart](#)

The Open University (UK)

190 PUBLICATIONS 3,996 CITATIONS

[SEE PROFILE](#)

Hippocampal circuit dysfunction in the Tc1 mouse model of Down syndrome

Jonathan Witton, Ragnathan Padmashri, Larissa E Zinyuk, Victor I Popov, Igor Kraev, Samantha J Line, Thomas P Jensen, Angelo Tedoldi, Damian M Cummings, Victor L J Tybulewicz, Elizabeth M C Fisher, David M Bannerman, Andrew D Randall, Jonathan T Brown, Frances A Edwards, Dmitri A Rusakov, Michael G Stewart & Matt W Jones

Abstract

Hippocampal pathology is likely to contribute to cognitive disability in Down syndrome, yet the neural network basis of this pathology and its contributions to different facets of cognitive impairment remain unclear. Here we report dysfunctional connectivity between dentate gyrus and CA3 networks in the transchromosomal Tc1 mouse model of Down syndrome, demonstrating that ultrastructural abnormalities and impaired short-term plasticity at dentate gyrus–CA3 excitatory synapses culminate in impaired coding of new spatial information in CA3 and CA1 and disrupted behavior *in vivo*. These results highlight the vulnerability of dentate gyrus–CA3 networks to aberrant human chromosome 21 gene expression and delineate hippocampal circuit abnormalities likely to contribute to distinct cognitive phenotypes in Down syndrome.

Introduction

Down syndrome (DS) results from trisomy of human chromosome 21 (Hsa21) and is the most common genetically defined cause of intellectual disability. However, the functions of many Hsa21 genes and the relative contributions of their overexpression to the diverse symptoms of DS remain undetermined. A range of aneuploid mouse models has been engineered to address this issue by linking trisomic overexpression of particular subsets of Hsa21 genes or their mouse orthologs to particular subsets of symptoms^{1,2,3}. Several of these mouse lines show hippocampal dysfunction and associated cognitive deficits, thereby corroborating clinical data suggesting that hippocampal abnormalities^{4,5,6,7} may be a root cause of some pre-dementia cognitive deficits—particularly in the realm of learning and memory—in DS^{8,9}.

Ts65Dn mice are the most widely studied DS model. They are partially trisomic for mouse chromosome 16, which has a region of conserved synteny with Hsa21, but their genetic basis in relation to DS is complicated by the trisomy of at least 60 non-DS-related genes on mouse chromosome 17 (refs. [10,11](#)). Ts65Dn mice display altered synaptic density, plasticity and excitatory–inhibitory balance in the hippocampus^{12,13,14} and abnormal synaptic morphology in the dentate gyrus (DG) and CA3 (refs. [15,16](#)). However, the net impact of DG–CA3 dysfunction on *in vivo* hippocampal circuit function, information coding and output via CA1 in Ts65Dn mice has not been ascertained. The Tc1 transchromosomal mouse line carries most of Hsa21 and is therefore a more direct model of trisomy 21. Tc1 mice also show phenotypic alterations in hippocampus-dependent behavior and synaptic plasticity in DG, alongside cerebellar, cardiovascular and craniofacial traits reminiscent of human DS^{17,18}. Taken together with findings in Ts65Dn mice, it therefore appears that DG

and CA3 networks may be selectively vulnerable to changes in expression of Hsa21 genes or their mouse orthologs.

DG and CA3 abnormalities are likely to affect the routing, storage and recall of information involving pattern separation and completion¹⁹. This processing relies on feedback loops between the two subregions, which incorporate excitatory projections from DG granule cells (GC) to the autoassociative CA3 pyramidal cell network via mossy fibers (MF), GC MF projections to CA3 GABAergic interneurons and CA3–DG feedback via back-projections to GCs, DG interneurons and excitatory mossy cells of the hilus. The tuning of these circuits enables strong but selective excitation of subsets of CA3 pyramidal cells by specific GC assemblies. MF axons form low-density, high-efficacy excitatory synapses that target specialized postsynaptic structures known as thorny excrescences on CA3 pyramidal cells. These synapses are characterized by marked facilitation in response to repetitive GC firing at short latencies and can thereby act as 'conditional detonator' synapses, inducing postsynaptic CA3 pyramidal cell spiking and consequent activation of connected CA1 cell ensembles only during particular patterns of GC activity²⁰.

Even subtle alterations of connectivity and excitatory–inhibitory balance in the DG–CA3 system are likely to confound accurate disambiguation or association of contextual (for example, spatial) and temporal information during pattern separation and completion, respectively, leading to impaired hippocampus-dependent episodic memory processing in DS and related diseases²¹. Using a combination of *in vitro* and *in vivo* imaging, and electrophysiological and behavioral analyses, we show that overexpression of Hsa21 genes leads to ultrastructural and neurophysiological synaptic changes in DG and CA3 networks, and that consequent CA1 dysfunction contributes to cognitive impairment in the Tc1 mouse model of DS.

Results

Impaired mossy fiber short-term plasticity in Tc1 mice

To survey core features of hippocampal excitatory synaptic transmission in Tc1 mice, we recorded extracellular field potentials evoked by MF or Schaffer collateral stimulation in hippocampal slices from adult Tc1 mice and age-matched, wild-type littermates. Baseline DG–CA3 transmission assessed using input-output curves was similar in Tc1 and wild-type mice (two-way mixed ANOVA, $F(1,19) = 0.59$, $P = 0.45$; [Fig. 1a](#)), as was DG granule cell excitability ([Supplementary Fig. 1](#)). However, a key physiological feature of MF transmission is pronounced short-term synaptic facilitation during repetitive stimulation. We investigated this phenomenon by delivering paired-pulse stimuli with inter-stimulus intervals (ISIs) increasing logarithmically from 10 to 1,000 ms. MF field EPSPs from Tc1 and wild-type mice exhibited pronounced paired-pulse facilitation (PPF) at all ISIs tested, but PPF was consistently reduced (by 5–20%) in Tc1 mice relative to wild-type controls (two-way mixed ANOVA, $F(1,19) = 7.02$, $P = 0.02$; [Fig. 1b](#)). MF synapses also classically show marked frequency facilitation to trains of presynaptic stimuli delivered at ~1 Hz. Synaptic facilitation during a 20-stimulus, 1-Hz train was strongly attenuated in Tc1 mice as compared to wild-type controls (two-way mixed ANOVA, $F(1,19) = 10.99$, $P = 0.004$; [Fig. 1c](#)), though the facilitation time constant was not different between the

genotypes (wild type, 3.04 ± 0.26 s (mean \pm s.e.m.); Tc1, 2.67 ± 0.31 s; unpaired *t*-test, $t(19) = 0.88$, $P = 0.39$).

In addition to MF short-term synaptic plasticity, we investigated NMDA receptor-independent long-term potentiation (LTP) at MF synapses in Tc1 and wild-type mice. LTP was induced using a 1-s, 100-Hz conditioning stimulus repeated three times at 10-s intervals (Fig. 1d). At 25–30 min after tetanization, we observed a stable LTP of $29.4 \pm 11\%$ and $32.8 \pm 8\%$ in wild-type and Tc1 mice, respectively (unpaired *t*-test, $t(6) = -0.25$, $P = 0.81$). The group II metabotropic glutamate receptor agonist DCG-IV ($2 \mu\text{M}$) was applied at the end of experiments to confirm that responses were predominantly MF driven²² (Fig. 1d).

In contrast to that at MF–CA3 synapses, short-term plasticity (PPF) at Schaffer collateral synapses between CA3 and CA1 pyramidal cells remained intact in Tc1 mice, and CA3–CA1 baseline transmission and LTP were also normal (Supplementary Fig. 2). Thus, while LTP appears intact in both CA3 and CA1, the short-term plasticity characteristic of MF-mediated responses is preferentially impaired in Tc1 mice, consistent with preferential dysfunction of MF–CA3 transmission in the Tc1 model. This short-term facilitation is likely to be central to the 'conditional detonator' properties of DG–CA3 connectivity, thereby tuning DG–CA3 interactions and downstream CA1 information processing during behavior.

Abnormal synapse density and ultrastructure in Tc1 mice

We used electron microscopy to characterize the structural underpinnings of hippocampal dysfunction in Tc1 mice, focusing on the DG–CA3 networks implicated by the brain slice electrophysiology described above. Hippocampus:brain volume ratios were normal in Tc1 mice relative to wild-type littermates (0.079 and 0.075 , respectively; Supplementary Fig. 3a), suggesting gross hippocampal anatomy to be consistent between the two genotypes. In the DG of Tc1 mice, overall GC densities were normal (Supplementary Fig. 3b), as was general synaptic organization of middle molecular layer (MML), where input from superficial layers of the entorhinal cortex forms excitatory synapses with GC dendritic spines. However, overall MML synapse density measured using three-dimensional reconstructions in a given tissue volume was significantly reduced in Tc1 mice (by 14.6% ; $P = 0.018$; Fig. 2a).

To establish whether the balance of MML synapse categories was altered in Tc1 mice, we classified spines as thin, stubby, mushroom or axo-dendritic according to their morphology and location. The proportions of all four subclasses of spines were normal in Tc1 mice (Fig. 2b). There were no statistically significant differences in volume or surface area of mushroom spines, the spine population that may represent mature synapses²³. However, three-dimensional reconstructions revealed that postsynaptic density (PSD) volumes of mushroom spines in the MML of Tc1 mice were significantly smaller than in wild type ($0.014 \pm 0.002 \mu\text{m}^3$ versus $0.021 \pm 0.002 \mu\text{m}^3$, respectively, $P = 0.011$; Fig. 2c–e). Overall, these results suggest reduced input from entorhinal cortex to DG in Tc1 mice.

CA3 pyramidal cell densities were normal in Tc1 mice (Supplementary Fig. 3c). However, changes in CA3 synaptic architecture in Tc1 mice were more pronounced than in DG, with proximal apical dendrites of CA3 pyramidal cells showing a

profound loss of postsynaptic thorny excrescences (compare serial sections [Fig. 3a–d](#) from wild type with [Fig. 3e–h](#) from Tc1), particularly evident in three-dimensional reconstructions of CA3 dendritic segments (compare [Fig. 3i](#) with [Fig. 3j](#); [Supplementary Fig. 4](#)). Thorn density was reduced from $3.8 \pm 0.7 \mu\text{m}^3$ in wild type to $1.54 \pm 0.32 \mu\text{m}^3$ in Tc1 CA3. Related effects on mossy fiber (MF) presynaptic giant boutons and PSDs are shown in [Supplementary Figure 4](#). Although average thorny excrescence volume was similar ($0.66 \pm 0.13 \mu\text{m}^3$ versus $0.72 \pm 0.10 \mu\text{m}^3$ in wild type and Tc1, respectively), the average volume of individual giant boutons was markedly decreased in Tc1 mice (to $1.54 \pm 0.32 \mu\text{m}^3$, versus $8.56 \pm 2.48 \mu\text{m}^3$ in wild type). Similarly, Tc1 PSDs were smaller and less complex than in wild-type CA3 ($0.009 \pm 0.002 \mu\text{m}^3$ versus $0.015 \pm 0.002 \mu\text{m}^3$, respectively).

The main ultrastructural differences between DG MF–CA3 synapses in Tc1 and wild-type mice are summarized schematically in [Supplementary Figure 5](#). These are likely to result in reduced direct excitation of CA3 pyramidal cells by input from DG GCs in the Tc1 DS model.

Imaging of mossy fiber input to CA3 pyramidal cells

To test whether perturbed synaptic connectivity in area CA3 of Tc1 mice could be detected in live cells, we examined fine dendritic structures in CA3 pyramidal cell dendrites using two-photon excitation imaging in acute hippocampal slices. Cells were held in whole-cell mode, loaded with a bright morphological tracer and showed robust synaptic responses throughout the experiments (see below and [Online Methods](#)). To minimize measurement bias, an unsupervised thresholding algorithm was used to calculate the maximum projection area of readily identifiable thorny excrescences per dendritic length in the first 15–20 μm of the primary apical dendrite and second-order dendrites next to the first bifurcation ([Fig. 4a–d](#); [Online Methods](#)). Average thorny excrescence area per unit dendritic length for the primary apical dendrite was $\sim 87\%$ greater in wild-type than in Tc1 CA3 pyramidal cells ($1.049 \pm 0.158 \mu\text{m}$ versus $0.560 \pm 0.065 \mu\text{m}$; $n = 13$ and 16 , respectively; unpaired t -test, $t(27) = 3.07$, $P = 0.011$, conservative with Welch correction; [Fig. 4e](#)). A similar, nearly twofold difference was found in the second-order dendrites next to the first bifurcation ($0.912 \pm 0.08 \mu\text{m}$ versus $0.494 \pm 0.049 \mu\text{m}$, $n = 23$ and $n = 28$, respectively; $t(49) = 4.64$, $P = 2.67 \times 10^{-4}$; [Fig. 4e](#)). These results confirm that ultrastructural synaptic abnormalities in Tc1 mice were not generated by the electron microscopy fixation process, and they appear profound enough to impair DG–CA3 functionality.

Reduced MF input to CA3 pyramidal neurons in Tc1 mice

To test whether the functional MF input to CA3 pyramidal cells paralleled structural changes, we recorded miniature excitatory postsynaptic currents (mEPSCs) from CA3 pyramids (whole-cell mode, $V_m = -70 \text{ mV}$) in the presence of $1 \mu\text{M}$ TTX. First, we measured the average overall frequency of mEPSCs as a basic indicator of the excitatory synaptic input. We found no differences between Tc1 and wild-type slices ($n = 11$ and 18 , respectively; $P = 0.843$). However, in addition to MF synapses, CA3 cells receive a powerful excitatory input from commissural fiber projections that might mask reductions in MF input. We therefore sought to measure the contribution

of MF synapses by using a classical pharmacological dissection, suppressing MF release function with DCG-IV²².

As expected, applying 2 μ M DCG-IV for 15 min to wild-type slices reduced the frequency of mEPSCs from 1.70 ± 0.4 Hz to 0.37 ± 0.1 Hz ($n = 10$ cells from 8 mice; $t(9) = -6.58$, $P = 1.01 \times 10^{-4}$; Fig. 5a). In slices from Tc1 mice, this frequency was reduced by DCG-IV from 1.67 ± 0.4 Hz to 0.69 ± 0.3 Hz ($n = 14$ cells from 9 mice; $t(13) = -4.71$, $P = 4.07 \times 10^{-4}$; Fig. 5b). We found that the average contribution of DCG-IV-sensitive mEPSCs (attributable to the MF connectivity of CA3 pyramidal cells) was significantly lower in Tc1 than wild-type mice (wild-type $79.9 \pm 3\%$ and Tc1 $59.0 \pm 8.7\%$ of all mEPSCs, respectively; $t(22) = 1.96$, $P = 0.037$, non-equal-variance t -test; Fig. 5c). This suggests that the relative weight of DG–CA3 synaptic connections (as compared to commissural ones) in the Tc1 sample was significantly lower than in the wild type. In addition, the variation of the DCG-IV effect among individual cells in the Tc1 mice was $\sim 30\%$ greater than in the wild type ($P < 0.005$, variance test). Indeed, one subgroup of sampled cells in the Tc1 mouse ($n = 5$) showed a markedly reduced effect of DCG-IV (Fig. 5c).

This bimodality in the Tc1 group of cells could be because Tc1 mice are mosaic for Hsa21, with different proportions of cells in different tissues carrying the extra chromosome; estimates of aneuploidy across whole brain range from 60–70% (ref. 17). To test whether the uneven distribution of the DCG-IV sensitivity reflects this mosaicism at structural and functional levels, we examined the relationship between the frequency of DCG-IV-sensitive mEPSCs and the expression of thorny excrescences documented in the same cells. This analysis revealed that the thorny area per dendritic length was indeed positively correlated with the magnitude of the DCG-IV effect in the same cell ($n = 7$, linear regression at $P = 0.035$; Fig. 5d), thus establishing a relationship between morphological and functional cell phenotypes. These data provide evidence that Hsa21 aneuploidy resulted in reduced morphological and functional connectivity in the MF–CA3 pyramidal cell circuitry.

MFs also project to GABAergic interneurons in CA3 (ref. 24), raising the possibility that altered DG–CA3 connectivity in Tc1 mice may also affect inhibitory circuitry. To assess this, live MF axons in acute brain slices from five Tc1 and five wild-type mice were electroporated with fluorescent dye to allow two-photon imaging of MF–interneuron presynaptic terminals (Fig. 5e; Online Methods). These MF–interneuron connections are structurally distinguishable from the giant boutons synapsing on pyramidal cells, appearing either as filopodium-like protrusions from MF giant boutons or as relatively small *en passant* boutons in MF axons²⁵. We found that Tc1 and wild-type MF displayed similar anatomy, with similar numbers of detectable filopodial boutons (per giant bouton, $P = 0.58$, rank sum test) and *en passant* boutons (per unit length of MF axon, $P = 0.75$, rank sum test) in the two genotypes (Fig. 5f). These structural data indicate that DG–CA3 inhibitory connections appear unaltered, in contrast to the impaired excitatory connections in Tc1 mice.

Impaired place cell coding in CA3 and CA1 of Tc1 mice

Aberrant DG–CA3 synaptic morphology and short-term plasticity in Tc1 mice are likely to impair spatial information processing both within CA3 and, consequently, in downstream circuits in CA1. We therefore used implanted tetrodes to record either

dorsal CA3 or CA1 place cell activity in freely moving Tc1 and wild-type mice as they explored a novel, 80-cm-long linear track (Fig. 6). These behavioral conditions are likely to recruit entorhinal–hippocampal systems underpinning spatial learning and memory.

CA3 pyramidal cells in Tc1 (52 cells from 3 mice) and wild-type mice (47 cells from 3 mice) exhibited comparable mean firing rates (0.9 ± 0.1 and 1.1 ± 0.2 Hz, respectively; $P = 0.15$, rank sum test). However, CA3 pyramidal cell activity was more spatially diffuse in Tc1 mice, with Tc1 place cell spiking covering $29 \pm 1.3\%$ and wild-type spiking $25 \pm 1.5\%$ of the linear track ($t(97) = -2.08$, $P = 0.039$, unpaired t -test; Fig. 6e–g).

Larger place fields in the absence of higher firing rates may stem from trial-by-trial instability in firing locations; this effect has recently been demonstrated in CA1 of the Tg4510 mouse model of dementia²⁶ and in mice lacking functional NMDA receptors in CA1 (ref. 27). Inter-trial spatial cross-correlations (given as median [interquartile range]) were slightly lower for Tc1 CA3 place cells (0.059 [–0.02 to 0.14]) than wild-type place cells (0.071 [–0.01 to 0.27]; $P = 0.049$, rank sum test; Fig. 6h), showing reduced stability of location-specific firing in Tc1 CA3, consistent with compromised input from upstream DG cell ensembles.

The activity of place cells is typically directionally sensitive on linear tracks, with firing rates conjunctively encoding both location and running direction. This directionality was quantified using a directional index (DI), defined as the magnitude of the difference between firing rates in the two directions divided by the sum of the two firing rates. DI therefore ranges between 0 for place cells that fire at identical rates in the two directions and 1 for cells that only fire in one of the two directions. In CA3, DI was similar for Tc1 (0.62 ± 0.04) and wild-type (0.60 ± 0.04) place cells ($t(97) = -0.31$, $P = 0.76$, unpaired t -test; Fig. 6i), indicating that at least some core features of CA3 spatial coding persist in Tc1 mice despite compromised DG input.

Aberrant CA3 place cell activity is likely to culminate in impaired spatial coding in CA1, where place cells are driven by convergent input from CA3 Schaffer collaterals and spatially modulated cells in the entorhinal cortex via the temporoammonic pathway. We isolated 50 putative CA1 pyramidal cells from Tc1 mice ($n = 7$ mice) and 63 from wild type ($n = 7$ mice) (mean cluster isolation distances 19 ± 1.6 and 15 ± 1.1 for Tc1 and wild type respectively; $P = 0.054$, unpaired t -test; Fig. 6c,d) during a single session on the linear track for each mouse. Consistent with the *in vitro* data showing normal excitability in CA1 of Tc1 hippocampal slices, mean pyramidal cell firing rates on the track were similar in Tc1 mice and wild-type littermates (1.8 ± 0.2 and 1.6 ± 0.1 Hz, respectively; $P = 0.55$, unpaired t -test), suggesting that overall CA1 excitability levels were not grossly affected by DG–CA3 changes. In line with our observations of CA3 place cell activity, however, CA1 pyramidal cell firing was more spatially diffuse (median place field sizes, 36% [32 to 39] and 30% [21 to 36] for Tc1 and wild type, respectively; $P = 0.0003$, rank sum test; Fig. 6g) and less stable from lap to lap in Tc1 mice (median inter-trial spatial cross-correlations, 0.044 [0.002 to 0.095] and 0.092 [0.001 to 0.29] for Tc1 and wild type, respectively; $P = 0.042$, rank sum test; Fig. 6h), suggesting that compromised CA3 place cell activity leads to downstream impairment in spatial coding in CA1 in Tc1 mice. Furthermore, DI for Tc1 CA1 place cells was 0.39 ± 0.04 , significantly lower than for wild-type ($0.60 \pm$

0.03; $t(98) = 3.31$, $P = 0.0013$, unpaired t -test; Fig. 6i). Therefore, alongside reduced spatial selectivity and stability, Tc1 CA1 place cell firing rates discriminate running direction less accurately than CA1 place cells in wild-type mice.

Impaired hippocampus-dependent behavior in Tc1 mice

Efficient spatial working memory performance (win-shift behavior) on the radial arm maze requires the ability to distinguish accurately between similar reward arms and between different visits to those arms, and is thus likely to rely on effective pattern separation and completion and on accurate spatial coding in place cell networks to disambiguate between overlapping events or episodes. This behavior depends in part on DG function, since it is disrupted by deletion of the GluN1(NR1) subunit of the NMDA receptor selectively from the GC of the DG²⁸, and was therefore chosen to probe DG–CA3-dependent behavior in Tc1 mice under linear track-running conditions related to those used for place cell recordings.

Tc1 mice ($n = 9$) were slower than wild-type littermates ($n = 11$) to attain an efficient level of spatial working memory performance on the radial maze task, with a significant main effect of block ($F(3,54) = 56.20$; $P = 1 \times 10^{-4}$) and, notably, a significant genotype-by-block interaction (Fig. 7; $F(3,54) = 3.36$; $P = 0.025$; Online Methods). This was independent of the age at which the animals were tested (all interactions $P > 0.20$, although overall performance was poorer in older animals; $F(1,18) = 8.18$; $P = 0.01$). Further investigation of the genotype-by-block interaction using analysis of simple main effects revealed that spatial working memory performance in the Tc1 mice was significantly impaired during the second block of testing ($F(1,18) = 10.78$; $P = 0.004$). There was also a nonsignificant trend toward impaired performance in block 3 ($F(1,18) = 2.96$; $P = 0.10$), but by block 4 Tc1 performance was similar to that of wild-type animals ($F(1,18) = 0.134$; $P = 0.72$).

To control for the possibility that differences in spatial working memory performance were due to differences in running speed (animals that run more slowly may experience a longer delay between choices, and thus experience a greater mnemonic demand), running times were recorded during trials 14–16 of the second training block. The total time to complete the trial and collect all six rewards was recorded and divided by the total number of arm choices made, giving a measure of performance speed in terms of time per choice. The performance speeds did not differ between groups (median [interquartile range]: wild-type, 26.0 s [22.3–28.9]; Tc1, 28.0 s [27.8–33.4], $P = 0.07$, rank sum test). Spatial working memory performance (choice accuracy) was impaired in the Tc1 mice during these trials (errors per trial: wild type, 0.42 ± 0.12 ; Tc1, 1.44 ± 0.52 ; $t(18) = 2.10$; $P = 0.05$). These behavioral data therefore corroborate conclusions from structural and neurophysiological studies of DG, CA3 and CA1 in the Tc1 mouse model of DS, showing that impaired activity and interactions in these hippocampal subfields culminate in cognitive dysfunction associated with overexpression of Hsa21 genes.

Discussion

Our ultrastructural analyses of DG MML and proximal dendrites of CA3 pyramidal cells in both fixed tissue and living cells reveal synapse loss and altered spine morphology in Tc1 mice strikingly reminiscent of that reported in the Ts65Dn mouse

model of DS¹⁶; this implicates altered expression of genes common to both models in triggering hippocampal abnormalities. Additional DS mouse models include Ts1Cje and Ts1Rhr mice, the latter being trisomic for only a Down-syndrome-critical subset of mouse genes triplicated in both Ts65Dn and Ts1Cje (ref. 29). Since the reduction of MML synapse density appears common to the Tc1, Ts65Dn and Ts1Rhr models, conserved syntenic regions of mouse chromosome 16 and Hsa21 may trigger this DG phenotype. Specific candidate genes include the dual-specificity protein kinase Dyrk1A, which is increasingly implicated in Alzheimer disease–related pathology in DS³⁰. However, since Tc1 mice unexpectedly fail to overexpress human amyloid precursor protein, the synaptic abnormalities described here can be categorically dissociated from A β -associated neurodegeneration. Tc1 mice therefore recapitulate hippocampal dendritic spine abnormalities seen in humans with DS before the onset of Alzheimer disease³¹ and present an opportunity to distinguish between DS and Alzheimer disease–related phenotypes.

Reduced DG MML synapse density, smaller PSD volumes and reduced presence of postsynaptic thorny excrescences are likely to underlie the reduced surface expression of the AMPA receptor subunit GluR1 seen in Tc1 mice¹⁸, presumably resulting in reduced excitatory synaptic drive of GCs by entorhinal cortical afferents via the medial perforant pathway. Despite this, we found no evidence for a compensatory increase in GC intrinsic excitability (Supplementary Fig. 1). The smaller mushroom spine PSDs in Tc1 mice are also consistent with attenuation of synaptic plasticity–induced synaptic enlargement²³ and may reflect the attenuated perforant path plasticity evident in Tc1 mice^{17,18}. Plasticity at perforant path–GC synapses is required for normal DG function—for example, underpinning pattern separation³². Thus, entorhinal cortex input to DG in this mouse model of DS appears severely compromised, and this is presumably a critical contributor to impaired CA3 and CA1 place cell function in Tc1 mice.

Behavioral data suggest that Tc1 hippocampal circuit abnormalities manifest preferentially during periods of enhanced demand for spatial memory processing. Tc1 mice have been reported to show normal learning in a standard version of the water maze and normal spontaneous alternation in a T-maze¹⁷, a rule- and reinforcement-free test of innate behavior, but show significant impairments in the six-arm radial arm maze task used here. This is consistent with impaired pattern separation and preferential retardation of more complex cognitive processing during conditions that require disambiguation of multiple rewarded locations and/or episodes and may therefore demand enhanced entorhinal cortex–DG recruitment. Further testing is required to determine whether Tc1 behavioral impairments also reflect load-dependent visuospatial working memory deficits, a phenotype observed in human DS³³. However, alongside evidence for DG hypocellularity in DS³⁴, over-inhibition of DG in Ts65Dn mice¹³ and impaired DG-dependent behavior in the Ts65Dn model³⁵, our study indicates that attenuated entorhinal cortex–DG synaptic function may be a central contributor to intellectual disabilities stemming from pattern separation failures. Whether or not direct entorhinal cortex input to CA1 via the temporoammonic pathway is also compromised in DS or DS models remains to be tested. It may be that unreliable spatial coding in CA1 of Tc1 mice stems from disrupted input from both the DG–CA3 network and temporoammonic pathway, creating a 'mismatch' between inputs from CA3 place cells and spatially modulated

cells in entorhinal cortex (that is, grid cells, border cells and head direction cells) during memory-guided behavior.

Different components of hippocampus-dependent information processing cannot be categorically assigned to single hippocampal subfields, and the trade-off between pattern separation and completion is mediated by the DG and its interactions with CA3 (refs. 19,36). Reduced synaptic drive of DG might be expected to lead to reduced downstream activation of CA3 in Tc1 mice, particularly when combined with the profound reduction in the number and complexity of MF–CA3 pyramidal cell excitatory synapses evident at the electron microscopy level. Our patch-clamp recordings from CA3 pyramidal cells combined with two-photon excitation imaging in acute slices showed a smaller proportion of MF-associated miniature excitatory events in Tc1 than in wild-type mice. This reduced drive by MF was correlated with reduced thorny excrescence volume in individual recorded cells (including those potentially carrying Hsa21, since Tc1 mice are mosaic for the transchromosome). These analyses point to attenuated DG–CA3 interactions as a central component of hippocampal dysfunction in Tc1 mice.

In addition to reduced basal MF input, our data show an impairment of MF short-term synaptic facilitation in Tc1 mice. This form of short-term plasticity is triggered by mechanisms dependent on presynaptic Ca^{2+} concentration. Its impairment may therefore reflect the reduced MF giant bouton volume shown here in Tc1 mice, although the abnormal postsynaptic excrescences may also contribute. The fact that NMDA receptor-independent LTP at MF synapses appeared intact in Tc1 mice (as it does in organotypic slices from the Ts65Dn mouse model of DS³⁷) supports the notion that Ca^{2+} from different sources may trigger the two forms of plasticity²², which may in turn make differential contributions to information processing. Nevertheless, attenuated MF short-term plasticity is likely to detract from detonator synapse function and exacerbate impaired information transfer across DG, CA3 and CA1 networks in Tc1 mice. A similar deficit in MF short-term potentiation has been identified in a transgenic mouse model of Alzheimer disease³⁸, and hence this phenotype may be more widely distributed in conditions associated with cognitive impairment.

DS is a systemic disease, and its cognitive symptoms are unlikely to stem solely from hippocampal dysfunction. Nevertheless, the central roles of the hippocampus in rapidly and accurately encoding, integrating or retrieving components of episodic memory do mean that any reduced or aberrant connectivity in hippocampal circuits is likely to prove disproportionately disruptive—particularly if present throughout the lifespan, as appears to be the case in DS^{4,5,6,7}. Abnormalities in DG and CA3 may be particularly disruptive, since their precisely connected and dynamically tuned networks act together to filter and associate information during mnemonic processing¹⁹. Commonalities across aneuploid mouse models of DS now point to overexpression of a subset of Hsa21 genes (not including amyloid precursor protein, responsible for Alzheimer disease-related neurodegeneration) driving a combination of reduced entorhinal cortex input to DG, abnormal DG–CA3 connectivity and consequently impaired information processing in CA3 and CA1 networks. These abnormalities are likely to preferentially impair cognition dependent on pattern separation and completion (for example, disambiguation between overlapping

competing memories), and cognitive testing in people with DS should be used to test this explicitly.

Finally, the impact of potential pharmacological therapies for cognition in DS³⁹ on DG–CA3–CA1 interactions should also be reconsidered: the network effects of targeting one hippocampal subfield (for example, normalization of reduced inhibition in DG⁴⁰) must be taken into account, and therapeutic approaches based on Alzheimer disease–associated cognitive impairments⁴¹ may not be well suited to treatment of pre-dementia DS. That said, potential pharmacological or behavioral therapies influencing DG neurogenesis^{42,43} may go some way to rebalancing the entorhinal-hippocampal networks that this study of Tc1 mice implicates as central to hippocampal abnormalities in DS.

Methods

Animals.

Experiments were performed in accordance with the UK Home Office Animals (Scientific Procedures) Act (1986) and institutional Ethical Committee guidelines. The transchromosomal mouse line Tc1 was generated as described elsewhere¹⁷. This trans-species aneuploid mouse line stably transmits a freely segregating, almost complete copy of Hsa21 in a C57BL/6J_129S8 (F2) genetic background. Tc1 and their wild-type littermates are obtained from the mating of C57BL/6J_129S8 (F1) Tc1 females with C57BL/6J_129S8 (F1) males. Animals were genotyped by PCR, weaned at 3 weeks and housed by gender and litter under standard conditions. Experiments were conducted on adult male mice during the light phase of a 12-h light/dark schedule (with lights on at 7:00 a.m.) unless stated otherwise.

Histology and electron microscopy.

Mice were anesthetized with sodium pentobarbital (100 mg/kg, i.p.) and transcardially perfused with 0.5% glutaraldehyde and 2% paraformaldehyde. For volume estimates, 50- μ m coronal sections were taken using a Leica vibratome and every fifth section mounted on gelatin-coated glass slides and stained using toluidine blue (0.5% for 1 min). Sections were dehydrated and mounted with DPX under cover glass and JPEG images were captured under a X1 objective. Full-field JPEG images were aligned and the contours of each section of brain and hippocampal region traced digitally and volumes computed.

For electron microscopy, coronal vibratome hippocampal sections (50 μ m thick) were cut and fixed further by immersion in 0.1 M sodium cacodylate buffer (pH 7.2–7.3) containing 2.5% glutaraldehyde for 1–2 h at room temperature, followed by three washes in 0.1 M sodium cacodylate buffer. Tissue was postfixed with 1% osmium tetroxide and 0.01% potassium dichromate in 0.1 M sodium cacodylate buffer for 1–1.5 h at room temperature. Serial sections were cut with a Diatome diamond knife, forming a ribbon of 800–1,000 serial sections in the knife bath. These were broken into series of 15–20 sections, collected on pioloform-coated slot grids and counterstained with saturated ethanolic uranyl acetate followed by Reynolds lead citrate. The series were examined with a JEOL 1010 electron microscope and photographed at a magnification of 6,000–10,000. Cross-sectioned axons, dendrites

and mitochondria spanning all sections provided a reference for initial alignment of serial sections. Section thickness was determined using the approach of Fiala and Harris⁴⁴.

Digitally scanned electron microscopy negatives (900 dpi) were aligned as JPEG images (software available from J. Fiala and K.M. Harris, <http://synapses.clm.utexas.edu/>). Alignments were made with full-field images. Contours of individual cells and their elements were traced digitally and computed to enable three-dimensional reconstructions. For synapse density analysis, 4 mice per group were analyzed with 1 series of 50 sections per animal, (~30 μm^3 of tissue for each). Analyses of variance (ANOVAs) followed by Bonferroni's or Tukey's unequal *N* honest significant differences tests were performed with Origin 7.0 (Northampton, MA). Data are presented as mean \pm s.e.m.

***In vitro* electrophysiology, preparation 1: two-photon excitation imaging and whole-cell recording.**

Acute hippocampal slices 280 μm thick were obtained from 6- to 10-week-old male Tc1 mice and wild-type littermates. Slices were prepared in ice-cold slicing solution containing (in mM) NaCl 60, sucrose 105, KCl 2.5, MgCl_2 7, NaH_2PO_4 1.25, NaHCO_3 26, CaCl_2 0.5, ascorbic acid 1.3, sodium pyruvate 3 and glucose 8 (300–310 mosM), stored in slicing solution at 34 °C for 20 min before being transferred to an interface chamber for storage in extracellular solution containing (in mM) NaCl 119, KCl 2.5, MgSO_4 1.3, NaH_2PO_4 1, NaHCO_3 26, CaCl_2 2, glucose 20 (adjusted to 295–305 mosM with glucose). All solutions were bubbled continuously with 95% O_2 /5% CO_2 . Slices were allowed to rest for at least 60 min before recordings started. For recording, slices were transferred to the submersion-type recording chamber and superfused, at room temperature (22–24 °C), with artificial cerebrospinal fluid saturated with 95% O_2 /5% CO_2 containing (in mM) NaCl 119, KCl 2.5, NaH_2PO_4 1, CaCl_2 2, MgSO_4 1.3, NaHCO_3 26, glucose 20 (pH 7.4, osmolarity 295–305 mosM).

Electrophysiology. Whole-cell recordings in CA3 pyramidal neurons were performed using 3–3.5 $\text{M}\Omega$ pipettes with an intracellular solution of (in mM) potassium gluconate 130, KCl 5, MgCl_2 2, HEPES 10, di-tris-phosphocreatine 10, Na-ATP 4, Na-GTP 0.4 (pH adjusted to 7.2 with KOH, 290–295 mosM). The morphological tracer Alexa Fluor 594 hydrazide (50 μM) was also included in the intracellular solution. Voltage clamp recordings of miniature EPSCs were made, with the mEPSCs recorded at -70 mV. Receptor agonists and antagonists purchased from Tocris Cookson (Bristol, UK) were added to the aCSF at the following concentrations (in μM): TTX 1, picrotoxin 100 and DCG-IV ((2*S*,2'*R*,3'*R*)-2-(2',3'-dicarboxycyclopropyl)glycine) 2. Recordings were performed with a Multiclamp 700B amplifier (Molecular Devices). Recording sweeps were collected at 5 kHz using WinWCP (Strathclyde Electrophysiology). mEPSCs were recorded over 15-min periods in control and treated conditions; data were then analyzed off-line using Mini-Analysis software (Synaptosoft). mEPSCs were detected if their amplitude was greater than the threshold of 5 pA, and considered for analysis if their rise time was shorter than their decay time. Fluorescent probes were purchased from Invitrogen.

Two-photon excitation fluorescence imaging. We used a Radiance 2000 imaging system (Zeiss-Bio-Rad) or Olympus Fluoview imaging system optically linked to a

Mai-Tai femtosecond pulse laser (Spectraphysics-Newport) and integrated with patch clamp electrophysiology. CA3 pyramidal cells loaded with 50 μM Alexa Fluor 594 were imaged as stacks of 30–60 optical sections in the Alexa Fluor 594 emission channel ($\lambda_x^{2P} = 800 \text{ nm}$), collected in image frame mode (512 pixels \times 512 pixels, 8-bit) in 0.5- μm steps (Fig. 4). To minimize any measurement bias, we calculated the visible (maximum projection) area of the identifiable thorny excrescences per dendritic length in the first 15–20 μm of (i) the primary apical dendrite and (ii) second-order dendrites next to the first bifurcation using an unsupervised thresholding algorithm. The algorithm divides the image into objects and background by initiating a test threshold and computing the average of the pixels at or below the threshold and pixels above. It then computes the average of those two, increments the threshold and repeats the process until threshold = (average background + average objects)/2. For figure illustration purposes, the image stacks were z -axis averaged with ImageJ routines (Wayne Rasband, ImageJ, US National Institutes of Health).

Visualization of live mossy fiber boutons by axonal electroporation of fluorescent tracer dyes. To visualize the morphology of mossy fiber giant boutons in acute hippocampal slice preparations, a modification of the electroporation method originally described by Nevian and Helmchen⁴⁵ was developed. As opposed to electroporating individual dentate granule cells with fluorescent dyes and tracing the axons to CA3, mossy fiber axons in CA3 stratum lucidum were directly loaded by electroporation. Slices were prepared and maintained as per preparation 1. The mossy fiber tract was routinely identified under DIC and a monopolar glass stimulating electrode (4–5 $\text{M}\Omega$ tip resistance) filled with intracellular solution supplemented with 1 mM Alexa Fluor 594 (to highlight the morphology of labeled boutons) and 1 mM of the Ca^{2+} sensitive dye Fluo-5F (to assess their viability) was positioned with the tip at a 45–90° angle to the edge of the tract facing toward the pyramidal cell layer. Once positioned, a 100-ms duration, –10 V electroporation pulse was delivered through a constant voltage stimulus isolation box (Digitimer, Welwyn Garden City, UK); multiple electroporation sites were used per slice until one or more MF boutons could be readily imaged. Boutons displaying morphology as observed in whole cell patch loaded granule cells⁴⁶ with little fluorescence in the Fluo 5F channel, indicating a low basal $[\text{Ca}^{2+}]_i$, were accepted for further investigation. Bouton morphology was imaged in frame scan mode as a stack of 30–60 frames taken in 0.25- μm steps, with a size of 512 \times 512 pixels and a pixel size of 0.05 μm . Numbers of *en passant* and filopodial axonal boutons were then counted using 3D stacks of images by an experimenter who was blinded to genotype until analysis was complete. Morphological criteria for bouton identification were consistent with detailed 3D reconstructions in fixed preparations²⁶ and with previous reports of live Alexa Fluor 594–filled MFs in acute slices⁴⁶.

***In vitro* electrophysiology, preparation 2: MF–CA3 field potential recordings.**

500- μm transverse hippocampal slices were prepared from male, 5- to 7-month-old Tc1 mice and wild-type littermate controls (mean 6 months). Briefly, animals were killed via cervical dislocation, the brain rapidly removed and placed into ice-cold, high-sucrose solution containing (in mM) sucrose 189, D-glucose 10, NaHCO_3 26, KCl 3, MgSO_4 5, CaCl_2 0.1, NaH_2PO_4 1.25 (295–305 mosM). The cerebellum and frontal cortex were removed and the brain was separated into the two hemispheres. The hippocampus was then removed from each hemisphere and sliced along its

transverse axis in ice-cold high-sucrose solution. Slices were stored in a submerged incubation chamber at 37 °C for 30 min and then at room temperature in aCSF containing (in mM) D-glucose 10, NaCl 124, KCl 3, NaHCO₃ 24, NaH₂PO₄ 1.25, MgSO₄ 1, CaCl₂ 2 (295–305 mosM). All solutions were continuously bubbled with 95% O₂/5% CO₂. Slices were allowed to rest for at least 60 min before recordings were made. For recording, slices were transferred to an interface-type recording chamber and superfused at 33 ± 1 °C with aCSF saturated with 95% O₂/5% CO₂.

Electrophysiology. Extracellular recordings were made from stratum lucidum using glass micropipettes (~3 MΩ) filled with aCSF. Mossy fiber (MF) field EPSPs were evoked by 100 μs electrical stimulation of the dentate gyrus granule cell layer using a concentric bipolar stimulating electrode (inner diameter 12.5 μm; Royem Scientific Ltd, Luton, UK) connected to an isolated stimulator box (Digitimer, Welwyn Garden City, UK). To determine the maximal MF fEPSP, we delivered a saturating 300-μA pulse. Subsequent stimuli were then delivered at the current capable of inducing half of the maximum response.

Short-term MF synaptic plasticity was investigated in two ways: first, we recorded paired-pulses delivered over a range of inter-stimulus intervals varying logarithmically over two orders of magnitude (10–1,000 ms); second, we measured the change in synaptic response to a 20-pulse, 1-Hz stimulus train. MF long-term potentiation (LTP) experiments were performed in the presence of 5 μM L689,560 (Tocris Cookson, Bristol, UK) to block NMDA receptor function. Baseline synaptic transmission was recorded to stimuli delivered every 30 s for at least 10 min. NMDA receptor-independent LTP was then induced by a conditioning stimulus consisting of a 1-s, 100-Hz train, repeated three times at 10-s intervals. LTP was followed for 30 min after tetanization.

Recordings were made using an AxoClamp2B amplifier (Molecular Devices, CA, USA; Scientifica, Uckfield, UK) in series with a secondary instrumentation amplifier (NPI, Tamm, Germany). Signals were amplified 2,000 times, low-pass filtered at 10 kHz and sampled at 50 kHz using Clampex 10.1 software (Molecular Devices). fEPSPs were confirmed as arising from MFs by bath application of 2 μM DCG-IV (Tocris Cookson); only fEPSPs reduced by ≥70% after 20 min DCG-IV application were included in analyses. Excitability of DG GCs was characterized by extracellularly recording compound action potentials in the GC layer of DG in response to antidromic activation of MFs by stimulation in area CA3; these experiments were performed in the presence of the kainate-type AMPA receptor antagonist NBQX (5 μM).

Data were analyzed off-line using Clampfit 10.1 (Molecular Devices). The maximum amplitude of the MF fEPSP was measured. *N*-values refer to experiments performed on a single slice taken from an individual animal. The Student's *t*-test and two-way ANOVA were used to test for significance where appropriate.

***In vitro* electrophysiology, preparation 3: Schaffer collateral–CA1 field potential recordings.**

For CA3–CA1 synaptic recordings, 400-μm transverse hippocampal slices were prepared from 9- to 12-week-old Tc1 mice and wild-type littermate controls. Animals

were killed by decapitation and the brain rapidly removed to ice cold slicing medium, containing (in mM) 125 NaCl, 2.4 KCl, 26 NaHCO₃, 1.4 NaH₂PO₄, 20 D-glucose, 3 MgCl₂, 0.5 CaCl₂, ~315 mosM. Slices were subsequently transferred at 5-min intervals to medium containing gradually more-physiological Ca²⁺ and Mg²⁺ concentrations (in mM Ca²⁺/Mg²⁺): (0.5/3; 0.5/1; 1/1; 2/1), maintained at 36 °C and saturated with 95% O₂/5% CO₂. Finally, slices were left to recover for >40 min in a submerged incubation chamber at room temperature. For recording, slices were transferred to a submerged recording chamber and superfused with saturated aCSF (slicing medium with 2 mM Ca²⁺ and 1 mM Mg²⁺, saturated with 95% O₂/5% CO₂ and maintained at 30 ± 1 °C).

Electrophysiology. Extracellular field recordings were made from stratum radiatum using glass micropipettes (~1.5 MΩ), filled with aCSF. Electrical stimulation was applied to Schaffer collateral fibers at 0.1 Hz via a glass stimulating electrode filled with aCSF placed in the stratum radiatum either anterograde or retrograde to the recording electrode and connected to an isolated constant voltage (100 μs) stimulator (Digitimer, UK). To determine the maximal fEPSP, a stimulus-response relationship was evoked between 10 and 80 V and subsequent stimulation intensity set at the lower intensity of either 30–50% maximum response or 30–50% of the threshold for a population spike. Long-term synaptic plasticity was examined by applying a tetanic stimulation, consisting of a 200-ms, 100-Hz train, repeated three times at 1.5-s intervals. LTP was followed for 1 h after conditioning.

Recordings were made using an AxoClamp 2B amplifier (Molecular Devices, CA, USA) with an HS-2A x1 headstage. 10Vm output signals were filtered at 10 kHz and subsequently amplified 100 times and low-pass filtered at 2 kHz (Frequency Devices 900 Filter) and then sampled at 10 kHz via an ITC16 digitizer connected to WinWCP software (Strathclyde Electrophysiology). fEPSP slope was measured from an average of six responses using the linear function within the Curve-Fit Analysis of WinWCP.

***In vivo* electrophysiology.**

Tetrode implants and surgery. Ten wild-type and ten Tc1 male mice (4–8 months; three of each genotype for CA3 recordings, seven of each for CA1) were implanted with four- to six-tetrode microdrives over the right dorsal hippocampus (centered 2.5 mm posterior to and 2.3 mm lateral from bregma for CA3, 1.5 mm lateral for CA1) under aseptic conditions and ketamine/xylazine recovery anesthesia. Each tetrode was spun from polyimide-insulated 13-μm nichrome wire (Kanthal, Hallstahammarm, Sweden). Drives were attached to the skull using gentamicin-impregnated Palacos R-40 cement and four stainless steel skull screws, one of which (over cerebellum) served as a ground connection for recording. After surgery, mice were individually housed with *ad libitum* access to food and water.

During the 7–20 d following surgery, the independently moveable tetrodes were lowered into either the CA3 or CA1 pyramidal cell layer (identified by the characteristic burst firing of single units and the presence of ripple or sharp-wave ripple events in local field potential) while mice occupied a small (15 × 15 cm base) holding box, set to one side of the linear track subsequently used for place cell recordings (see below). Extracellular action potentials (sampled at 30 kHz and filtered

between 0.6 and 6 kHz) were recorded differentially via a unity gain HS-18 preamplifier and Digital Lynx (Neuralynx, MT) using local references. In a subset of mice, tetrode tip positions were verified post mortem.

Recording setup. Recordings were made on an 80-cm-long, 5-cm-wide linear track with open 9-cm-high walls and a turning zone (10 × 10 cm) at each end, located in the middle of a room. All data were recorded during each mouse's first, novel exposure to the track. The linear track was made from dark gray plastic. Half of the white room walls were exposed and half covered by a black curtain; three-dimensional cardboard cues were hung to create a distinct spatial context. Eight regularly spaced incandescent bulbs were hung overhead to dimly illuminate the room. Video tracking sampled the positions of green and red LEDs attached to the preamplifier at 60 Hz, with a final resolution of approximately 1.5 cm.

Tetrode data analysis. All analyses were performed blind to genotype in MATLAB (MathWorks, MA). Spikes were sorted semi-automatically on the basis of waveform characteristics (amplitude and energy) using KlustaKwik 1.5 (K.D. Harris, <http://klustakwik.sourceforge.net/>), and clusters were then refined manually with MClust in MATLAB (A.D. Redish, <http://redishlab.neuroscience.umn.edu/>). Only units with less than 1% of inter-spike intervals below 2 ms and cluster isolation distances above 10 were selected for further analysis⁴⁷; cells with mean firing rates between 0.1 and 5 Hz on the linear track were considered putative pyramidal cells. Trial-by-trial positional firing correlations were calculated as described by Cheng and Ji (2013)²⁶, using 4-cm positional bins and excluding the turning zones at each end of the track; only cells with firing rates of at least 0.1 Hz in both running directions were included in this trial-by-trial analysis, with trials that took longer than 20 s excluded. The extent of spatial firing was based on firing rate maps on the linear track³².

Radial arm maze.

This study employed precisely the same maze, housed in the same facility, as that used by Niewoehner *et al.*²⁸ to demonstrate the dependence of task performance on normal DG function²⁷.

Wild-type ($n = 11$) and Tc1 ($n = 9$) mice were trained on a spatial working memory version of the radial maze task. Mice were first habituated to drinking a sweetened, condensed milk reward in their home cages, then habituated to drinking milk on an elevated Y-maze in their colony holding room (i.e., not the room used for spatial memory testing). The Y-maze consisted of three identical wooden arms, each 50 cm long by 9 cm wide, with a low white plastic wall (0.5 cm), connected by a central polygonal platform (14 cm diameter). The maze was painted black. A food well was positioned at the end of each arm.

The radial maze was made of wood and painted gray. It consisted of six arms (60 cm × 7 cm) radiating out from a central platform. Each arm was surrounded by a 1-cm raised edge and contained a food well located at the end. The central platform was surrounded by a transparent plastic cylinder (18 cm diameter, 30 cm high). At the entrance to each arm, a transparent plastic door (6 cm wide, 7 cm high) could be controlled manually by the experimenter using a series of strings. The maze was

positioned 80 cm above the floor and was surrounded by prominent distal extramaze cues.

To specifically assess hippocampus-dependent, spatial working memory, all six arms were baited with 0.05 ml sweetened condensed milk. At the start of each trial, the mouse was placed on the central platform and given a free choice of arms. After visiting the food well in the chosen arm and consuming the milk reward, the mouse would return to the central platform. Doors were used to contain the animals on the central platform between choices and thus prevent the use of simple mediating strategies. After 10 s, all doors were then reopened and the mouse allowed another choice. This was repeated until the mouse had visited all of the baited arms. Each entry into an arm that had previously been visited on that trial (and was now unbaited) was scored as a spatial working memory error.

Mice received one trial per day for a total of 24 d. Each mouse was tested twice: first at an age of 5–6 months and then again at 18 months of age. Data were collected in six trial blocks for analysis.

Statistical analyses.

Data sets were tested for normality and parametric or non-parametric, two-sided tests used as appropriate with an α of 0.05. Where appropriate, two-way analysis of variance (ANOVA) was used to compare data sets across multiple factors. *Post hoc* comparisons were made using a Bonferroni correction for multiple comparisons. Sample sizes were not formally predetermined using power calculations, but are consistent with previous studies combining *in vitro*, *in vivo* and behavioral measures³² and designed to enable detection of at least a 15% difference in the population mean at a $P < 0.05$ level given the sampled population variance. Imaging and electrophysiological data were collected from Tc1 and WT mice in randomized order and quantified blind to genotype. Most data are presented as mean \pm s.e.m.; where medians are presented for non-normally distributed data, the interquartile range is given in square brackets (median [IQR]).

References

1. Reeves, R.H. *et al.* A mouse model for Down syndrome exhibits learning and behaviour deficits. *Nat. Genet.* 11, 177–184 (1995).
2. Yu, T. *et al.* A mouse model of Down syndrome trisomic for all human chromosome 21 syntenic regions. *Hum. Mol. Genet.* 19, 2780–2791 (2010).
3. Pereira, P.L. *et al.* A new mouse model for the trisomy of the *Abcg1–U2af1* region reveals the complexity of the combinatorial genetic code of down syndrome. *Hum. Mol. Genet.* 18, 4756–4769 (2009).
4. Kesslak, J.P., Nagata, S.F., Lott, I. & Nalcioglu, O. Magnetic resonance imaging analysis of age-related changes in the brains of individuals with Down's syndrome. *Neurology* 44, 1039–1045 (1994).
5. Raz, N. *et al.* Selective neuroanatomic abnormalities in Down's syndrome and their cognitive correlates: evidence from MRI morphometry. *Neurology* 45, 356–366 (1995).

6. Aylward, E.H. *et al.* MRI volumes of the hippocampus and amygdala in adults with Down's syndrome with and without dementia. *Am. J. Psychiatry* 156, 564–568 (1999).
7. Pinter, J.D., Eliez, S., Schmitt, J.E., Capone, G.T. & Reiss, A.L. Neuroanatomy of Down's syndrome: a high-resolution MRI study. *Am. J. Psychiatry* 158, 1659–1665 (2001).
8. Pennington, B.F., Moon, J., Edgin, J., Stedron, J. & Nadel, L. The neuropsychology of Down syndrome: evidence for hippocampal dysfunction. *Child Dev.* 74, 75–93 (2003).
9. Edgin, J.O. *et al.* Development and validation of the Arizona Cognitive Test Battery for Down syndrome. *J. Neurodev. Disord.* 2, 149–164 (2010).
10. Duchon, A. *et al.* Identification of the translocation breakpoints in the Ts65Dn and Ts1Cje mouse lines: relevance for modeling Down syndrome. *Mamm. Genome* 22, 674–684 (2011).
11. Reinholdt, L.G. *et al.* Molecular characterization of the translocation breakpoints in the Down syndrome mouse model Ts65Dn. *Mamm. Genome* 22, 685–691 (2011).
12. Kurt, M.A., Kafa, M.I., Dierssen, M. & Davies, D.C. Deficits of neuronal density in CA1 and synaptic density in the dentate gyrus, CA3 and CA1, in a mouse model of Down syndrome. *Brain Res.* 1022, 101–109 (2004).
13. Kleschevnikov, A.M. *et al.* Hippocampal long-term potentiation suppressed by increased inhibition in the Ts65Dn mouse, a genetic model of Down syndrome. *J. Neurosci.* 24, 8153–8160 (2004).
14. Belichenko, P.V. *et al.* Excitatory-inhibitory relationship in the fascia dentata in the Ts65Dn mouse model of Down syndrome. *J. Comp. Neurol.* 512, 453–466 (2009).
15. Belichenko, P.V. *et al.* Synaptic structural abnormalities in the Ts65Dn mouse model of Down Syndrome. *J. Comp. Neurol.* 480, 281–298 (2004).
16. Popov, V.I., Kleschevnikov, A.M., Klimenko, O.A., Stewart, M.G. & Belichenko, P.V. Three-dimensional synaptic ultrastructure in the dentate gyrus and hippocampal area CA3 in the Ts65Dn mouse model of Down syndrome. *J. Comp. Neurol.* 519, 1338–1354 (2011).
17. O'Doherty, A. *et al.* An aneuploid mouse strain carrying human chromosome 21 with Down syndrome phenotypes. *Science* 309, 2033–2037 (2005).
18. Morice, E. *et al.* Preservation of long-term memory and synaptic plasticity despite short-term impairments in the Tc1 mouse model of Down syndrome. *Learn. Mem.* 15, 492–500 (2008).
19. Rolls, E.T. A computational theory of episodic memory formation in the hippocampus. *Behav. Brain Res.* 215, 180–196 (2010).
20. Henze, D.A., Wittner, L. & Buzsaki, G. Single granule cells reliably discharge targets in the hippocampal CA3 network *in vivo*. *Nat. Neurosci.* 5, 790–795 (2002).
21. Hanson, J.E. & Madison, D.V. Imbalanced pattern completion vs. separation in cognitive disease: network simulations of synaptic pathologies predict a personalized therapeutics strategy. *BMC Neurosci.* 11, 96 (2010).
22. Nicoll, R.A. & Schmitz, D. Synaptic plasticity at hippocampal mossy fiber synapses. *Nat. Rev. Neurosci.* 6, 863–876 (2005).
23. Bourne, J.N. & Harris, K.M. Coordination of size and number of excitatory and inhibitory synapses results in a balanced structural plasticity along mature hippocampal CA1 dendrites during LTP. *Hippocampus* 21, 354–373 (2011).

24. Acsády, L., Kamondi, A., Sik, A., Freund, T. & Buzsáki, G. GABAergic cells are the major postsynaptic targets of mossy fibers in the rat hippocampus. *J. Neurosci.* 18, 3386–3403 (1998).
25. Scott, R., Lalic, T., Kullmann, D.M., Capogna, M. & Rusakov, D.A. Target-cell specificity of kainate autoreceptor and Ca²⁺-store-dependent short-term plasticity at hippocampal mossy fiber synapses. *J. Neurosci.* 28, 13139–13149 (2008).
26. Cheng, J. & Ji, D. Rigid firing sequences undermine spatial memory codes in a neurodegenerative mouse model. *Elife* 2, e00647 (2013).
27. Cabral, H.O. *et al.* Oscillatory dynamics and place field maps reflect hippocampal ensemble processing of sequence and place memory under NMDA receptor control. *Neuron* 81, 402–415 (2014).
28. Niewoehner, B. *et al.* Impaired spatial working memory but spared spatial reference memory following functional loss of NMDA receptors in the dentate gyrus. *Eur. J. Neurosci.* 25, 837–846 (2007).
29. Belichenko, N.P. *et al.* The “Down syndrome critical region” is sufficient in the mouse model to confer behavioral, neurophysiological, and synaptic phenotypes characteristic of Down syndrome. *J. Neurosci.* 29, 5938–5948 (2009).
30. Park, J., Song, W.J. & Chung, K.C. Function and regulation of Dyrk1A: towards understanding Down syndrome. *Cell. Mol. Life Sci.* 66, 3235–3240 (2009).
31. Ferrer, I. & Gullotta, F. Down's syndrome and Alzheimer's disease: dendritic spine counts in the hippocampus. *Acta Neuropathol.* 79, 680–685 (1990).
32. McHugh, T.J. *et al.* Dentate gyrus NMDA receptors mediate rapid pattern separation in the hippocampal network. *Science* 317, 94–99 (2007).
33. Lanfranchi, S., Carretti, B., Spano, G. & Cornoldi, C. A specific deficit in visuospatial simultaneous working memory in Down syndrome. *J. Intellect. Disabil. Res.* 53, 474–483 (2009).
34. Guidi, S. *et al.* Neurogenesis impairment and increased cell death reduce total neuron number in the hippocampal region of fetuses with Down syndrome. *Brain Pathol.* 18, 180–197 (2008).
35. Smith, G.K., Kesner, R.P. & Korenberg, J.R. Dentate gyrus mediates cognitive function in the Ts65Dn/DnJ mouse model of down syndrome. *Hippocampus* 24, 354–362 (2014).
36. Jones, M.W. & McHugh, T.J. Updating hippocampal representations: CA2 joins the circuit. *Trends Neurosci.* 34, 526–535 (2011).
37. Hanson, J.E., Blank, M., Valenzuela, R.A., Garner, C.C. & Madison, D.V. The functional nature of synaptic circuitry is altered in area CA3 of the hippocampus in a mouse model of Down's syndrome. *J. Physiol. (Lond.)* 579, 53–67 (2007).
38. Witton, J., Brown, J.T., Jones, M.W. & Randall, A.D. Altered synaptic plasticity in the mossy fiber pathway of transgenic mice expressing mutant amyloid precursor protein. *Mol. Brain* 3, 32 (2010).
39. Gardiner, K.J. Molecular basis of pharmacotherapies for cognition in Down syndrome. *Trends Pharmacol. Sci.* 31, 66–73 (2010).
40. Fernandez, F. *et al.* Pharmacotherapy for cognitive impairment in a mouse model of Down syndrome. *Nat. Neurosci.* 10, 411–413 (2007).

41. Kishnani, P.S. *et al.* Donepezil for treatment of cognitive dysfunction in children with Down syndrome aged 10–17. *Am. J. Med. Genet.* 152A, 3028–3035 (2010).
42. Conners, F.A., Rosenquist, C.J., Arnett, L., Moore, M.S. & Hume, L.E. Improving memory span in children with Down syndrome. *J. Intellect. Disabil. Res.* 52, 244–255 (2008).
43. Contestabile, A., Benfenati, F. & Gasparini, L. Communication breaks-Down: from neurodevelopment defects to cognitive disabilities in Down syndrome. *Prog. Neurobiol.* 91, 1–22 (2010).
44. Fiala, J.C. & Harris, K.M. Cylindrical diameters method for calibrating section thickness in serial electron microscopy. *J. Microsc.* 202, 468–472 (2001).
45. Nevian, T. & Helmchen, F. Calcium indicator loading of neurons using single-cell electroporation. *Pflugers Arch.* 454, 675–688 (2007).
46. Scott, R. & Rusakov, D.A. Main determinants of presynaptic Ca²⁺ dynamics at individual mossy fiber-CA3 pyramidal cell synapses. *J. Neurosci.* 26, 7071–7081 (2006).
47. Schmitzer-Torbert, N., Jackson, J., Henze, D., Harris, K. & Redish, A.D. Quantitative measures of cluster quality for use in extracellular recordings. *Neuroscience* 131, 1–11 (2005).

Acknowledgments

Thanks to A. Slender, H. Davies and D. Ford for expert technical assistance and to the Wellcome Trust (Programme Grant to E.M.C.F., V.L.J.T. and M.W.J., Principal Fellowship to D.A.R.), the UK Medical Research Council (grant to E.M.C.F. and V.L.J.T., Industrial Collaborative Studentship to J.W.), Biotechnology and Biological Sciences Research Council (grant to M.G.S.), European Research Council Advanced Grant and FP7 ITN Extrabrain (to D.A.R.) Russian Science Foundation grant 15-14-30000 (to D.A.R.) and Russian Foundation for Basic Research grant 08-04-00049a (to V.I.P.) for financial support.

Author footnotes

- 1. Present address: University of Nebraska Medical Center, Omaha, Nebraska, USA.**
 - Rangunathan Padmashri
- 2. Deceased.**
 - Victor I Popov
- 3. These authors contributed equally to this work.**
 - Jonathan Witton,
 - Rangunathan Padmashri &
 - Larissa E Zinyuk

Affiliations

- 1. School of Physiology & Pharmacology, University of Bristol, Bristol, UK.**
 - Jonathan Witton,
 - Larissa E Zinyuk,
 - Andrew D Randall,

- Jonathan T Brown &
- Matt W Jones
- 2. Department of Clinical and Experimental Epilepsy, UCL Institute of Neurology, University College London, London, UK.**
 - Rangunathan Padmashri,
 - Thomas P Jensen &
 - Dmitri A Rusakov
- 3. Institute of Cell Biophysics, Russian Academy of Sciences, Pushchino, Moscow, Russia.**
 - Victor I Popov
- 4. The Open University, Department of Life Sciences, Milton Keynes, UK.**
 - Victor I Popov,
 - Igor Kraev &
 - Michael G Stewart
- 5. Laboratory of Brain Microcircuits, Institute of Biology and Biomedicine, University of Nizhny Novgorod, Nizhny Novgorod, Russia.**
 - Igor Kraev &
 - Dmitri A Rusakov
- 6. Department of Experimental Psychology, University of Oxford, Oxford, UK.**
 - Samantha J Line &
 - David M Bannerman
- 7. Department of Neuroscience, Physiology and Pharmacology, University College London, London, UK.**
 - Angelo Tedoldi,
 - Damian M Cummings &
 - Frances A Edwards
- 8. Francis Crick Institute, Mill Hill Laboratory, London, UK.**
 - Victor L J Tybulewicz
- 9. Imperial College, London, UK.**
 - Victor L J Tybulewicz
- 10. Department of Neurodegenerative Disease, UCL Institute of Neurology, University College London, London, UK.**
 - Elizabeth M C Fisher

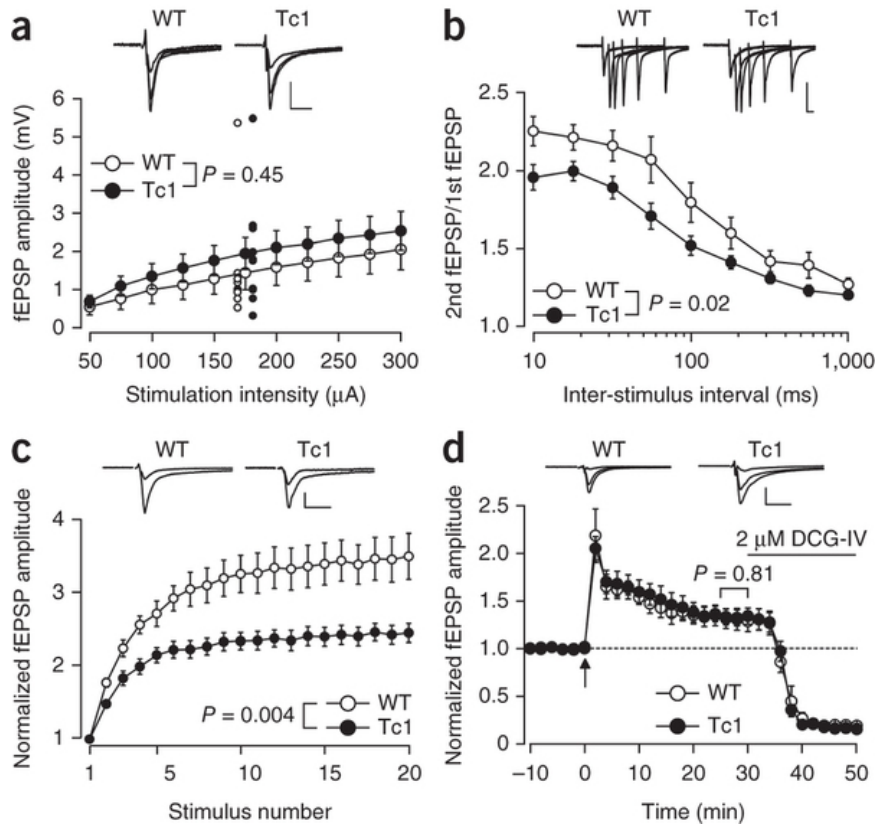
Contributions E.M.C.F. and V.L.J.T. designed the Tc1 mouse model and initiated the study. J.W., D.M.C. and A.T. performed extracellular *in vitro* electrophysiology and analyses; V.I.P. and I.K. performed electron microscopy and volumetric experiments and analyses; R.P. and T.P.J. performed two-photon imaging and intracellular electrophysiological recording and analyses; J.W. and L.E.Z. performed *in vivo* electrophysiology and analyses; S.J.L. performed behavioral experiments and analyses; and J.T.B., A.D.R., D.M.B., F.A.E., M.G.S., D.A.R. and M.W.J. designed experiments, performed data analyses and wrote the paper.

Competing financial interests

The authors declare no competing financial interests.

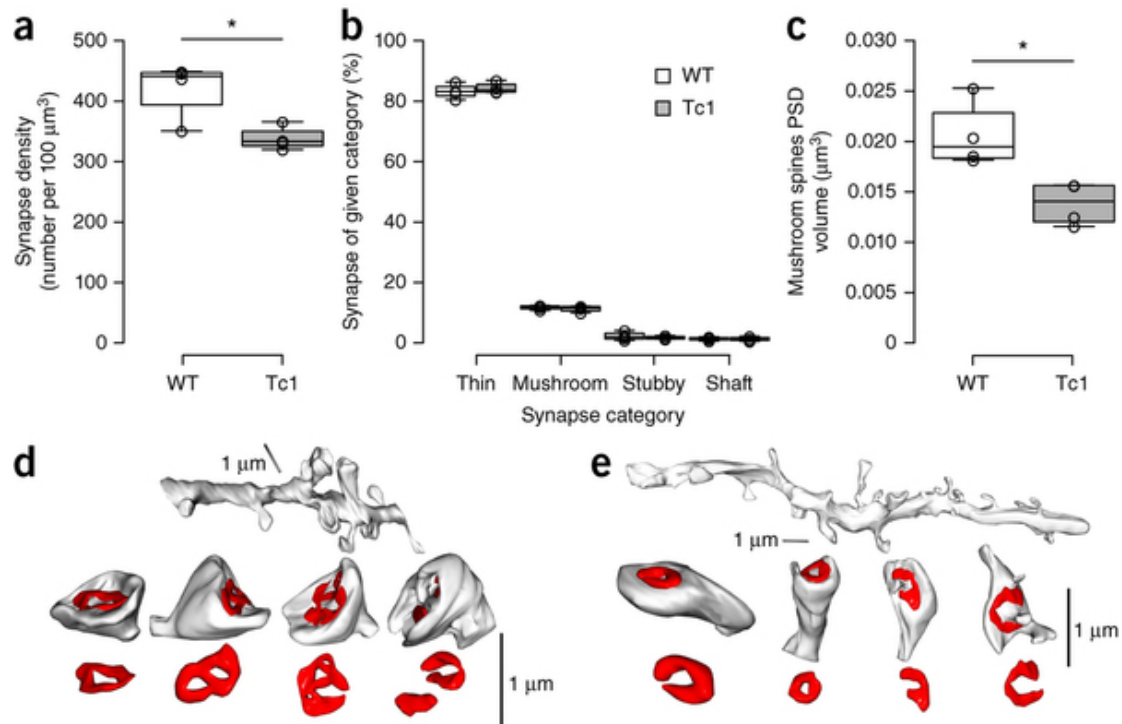
Corresponding author Matt W Jones

Figure 1: Altered short-term but not long-term synaptic potentiation in the mossy fiber pathway of Tc1 mice.



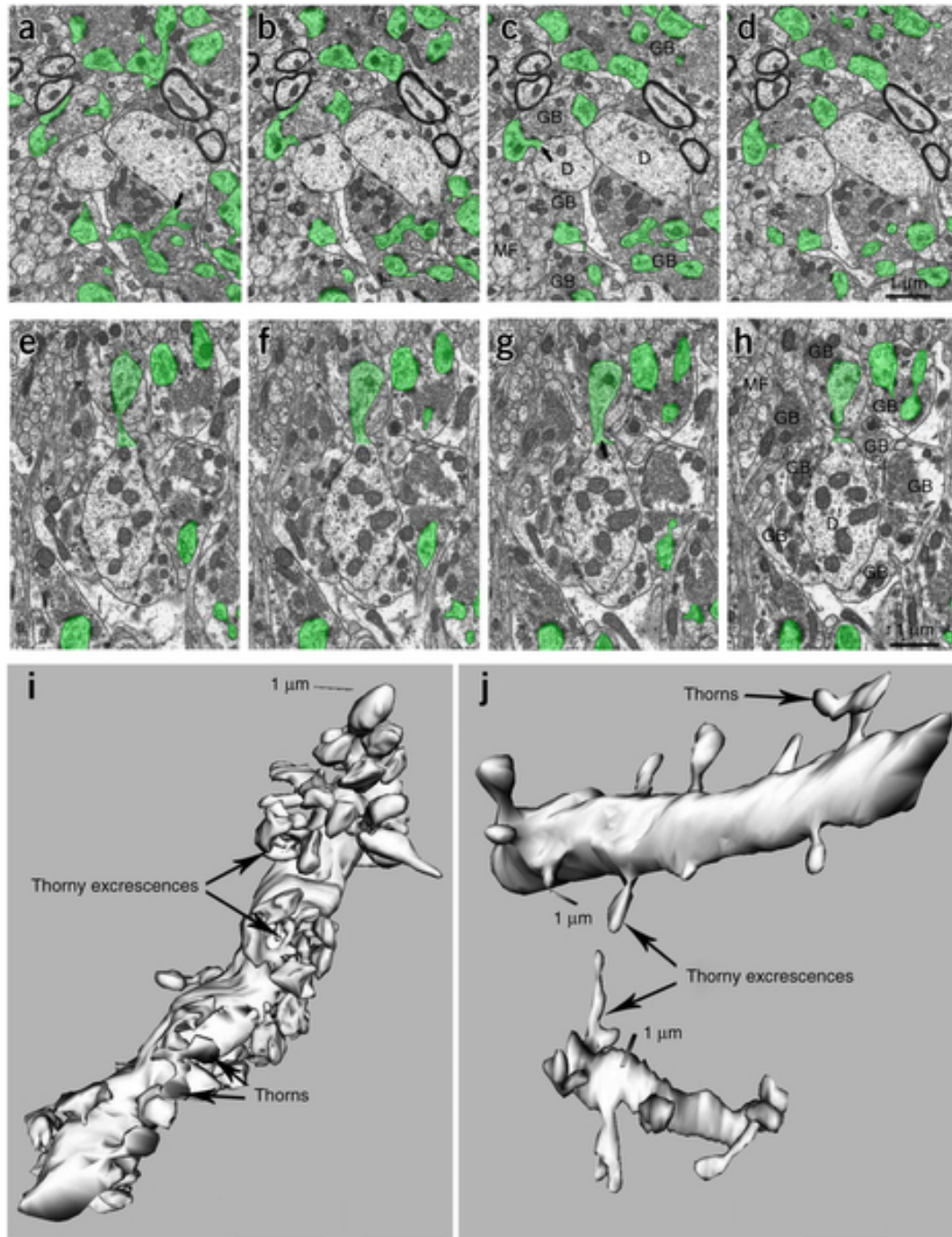
(a) Pooled MF-CA3 stimulus-response curves in hippocampal slices from wild-type (WT, $n = 10$) and Tc1 ($n = 11$) mice ($P = 0.45$, two-way ANOVA). Smaller circles show field excitatory postsynaptic potential (fEPSP) amplitudes in response to 175 μ A stimulation for individual mice to illustrate the spread of the data. Inset traces illustrate overlaid example responses to 50, 150 and 300 μ A stimulation for the two genotypes. Scale bars: 10 ms, 0.5 mV. (b) Pooled data for MF paired-pulse facilitation over inter-stimulus intervals from 10 to 1,000 ms ($P = 0.02$, two-way ANOVA). Example traces illustrate responses to paired stimuli delivered over inter-stimulus intervals of 10–100 ms, with a quarter log spacing. Scale bars: 10 ms, 0.5 mV. (c) MF frequency facilitation during a 1-Hz train of 20 pulses ($P = 0.004$, two-way ANOVA). The y ordinate plots the amplitude of the n th fEPSP of the train normalized to the amplitude of the first response. Example traces show overlaid recordings of the first and twentieth traces from wild-type and Tc1 mice. Scale bars: 10 ms, 0.5 mV. (d) Pooled MF LTP data from 4 wild-type and 4 Tc1 mice ($P = 0.81$, unpaired t -test). Arrow denotes timing of tetanic stimulation (1 s, 100 Hz repeated three times at 10-s intervals). fEPSP amplitude was recorded for 30 min following tetanization to measure LTP. Suppression following application of 2 μ M DCG-IV confirmed that fEPSPs were predominantly driven by MFs. Example traces show recordings from wild-type and Tc1 mice at 0 min, 30 min and 50 min. Scale bars: 10 ms, 0.5 mV. Symbols and error bars show mean \pm s.e.m.

Figure 2: Reduced synapse density and PSD volume in the middle molecular layer of dentate gyrus in Tc1 mice.



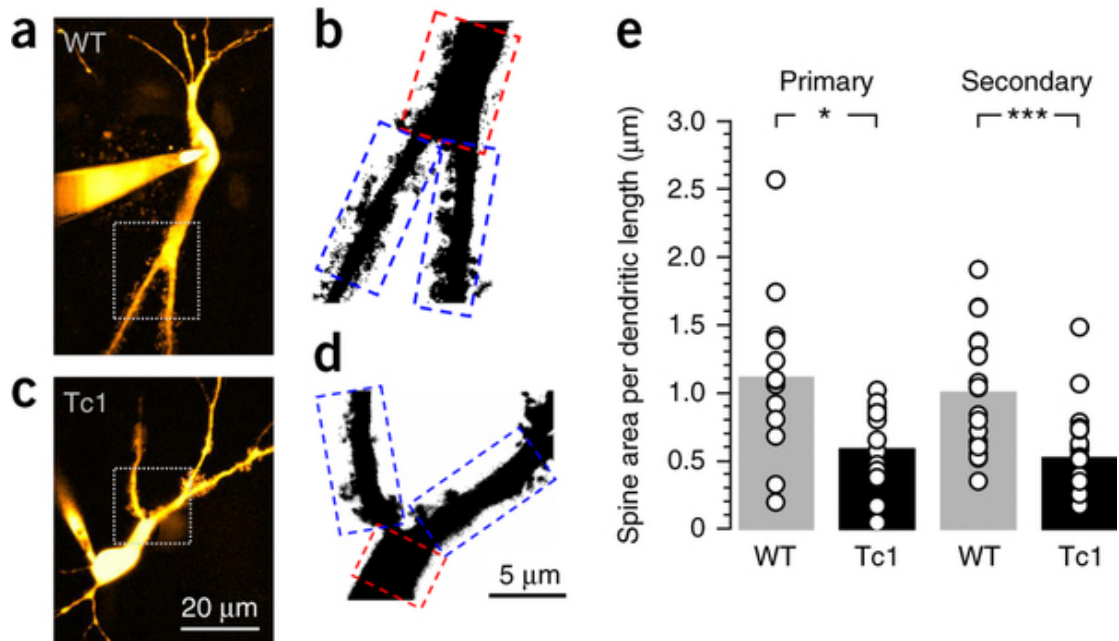
(a) Overall synapse densities per 100 μm^3 ($*P = 0.02$, ANOVA), (b) distributions of four categories of spine and (c) PSD volumes ($*P = 0.01$, ANOVA) in wild-type (WT, $n = 4$) and Tc1 mice ($n = 4$). Values for individual mice (open circles) are overlaid on box-and-whisker plots; center lines show the median, box limits illustrate the 25th and 75th percentiles and whiskers extend to the minimum and maximum values. (d,e) Three-dimensional reconstructions of dendritic segments and their mushroom spines with PSDs (red) in WT (d) and Tc1 (e) mice, exemplifying reduced PSD volumes in Tc1 animals.

Figure 3: Three-dimensional reconstruction of CA3 pyramidal cell dendrites reveals loss of thorny excrescences in Tc1 mice.



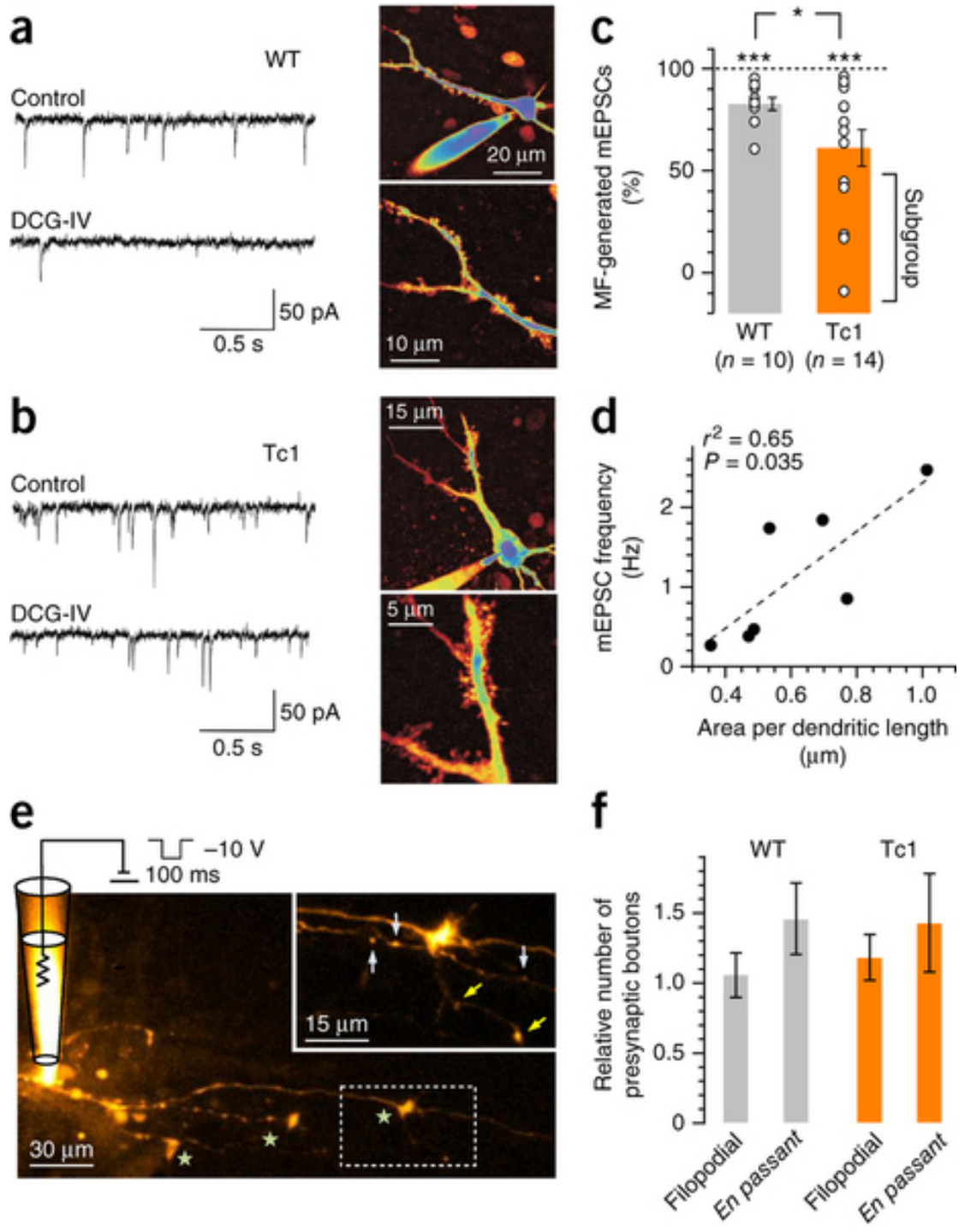
(a-h) Consecutive images of proximal portions of CA3 dendrites for wild-type **(a-d)** and Tc1 **(e-h)** mice. Thorny excrescence profiles are labeled in green, exemplifying a reduction of thorns in Tc1 mice. D, dendritic shafts; GB, mossy fiber giant boutons, or varicosities representing presynaptic portions of the synapses; MF, mossy fibers, or axons originating from granule cells. Arrows show thorns and thorny excrescences. **(i,j)** Three-dimensionally reconstructed CA3 dendritic segments with thorny excrescences in wild-type **(i)** and Tc1 **(j)** mice.

Figure 4: Adult Tc1 mice show reduced postsynaptic thorny excrescences in live CA3 pyramidal cells.



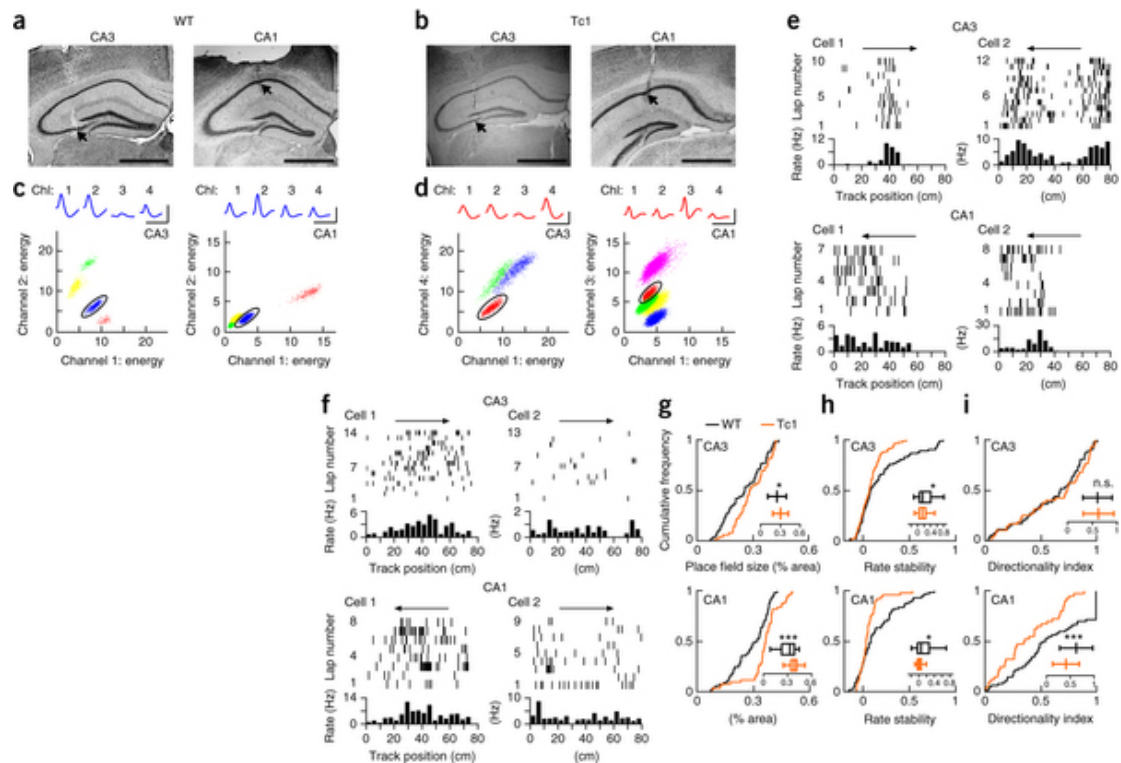
(a) An example of a wild-type (WT) CA3 pyramidal cell held in whole-cell mode (50 μM Alexa Fluor 594; two-photon excitation wavelength 800 nm). (b) The proximal dendritic segment of interest (marked in a by rectangle), with an unsupervised threshold applied. Red and blue dashed rectangles show the primary apical dendrite and second-order dendrites, respectively, used for assessing the extent of thorny excrescences. (c,d) Examples as in a,b, but from a Tc1 mouse. (e) Individual (open circles) and mean (bars) area per dendritic length for thorny excrescences in primary dendrites ($n = 13$ and 16 cells for wild type and Tc1, respectively; $*P = 0.01$, unpaired t -test) and secondary dendrites ($n = 23$ and 28 ; $***P = 2.7 \times 10^{-4}$).

Figure 5: Reduced contribution of mossy fiber input to CA3 pyramidal cell mEPSCs in Tc1 mice.



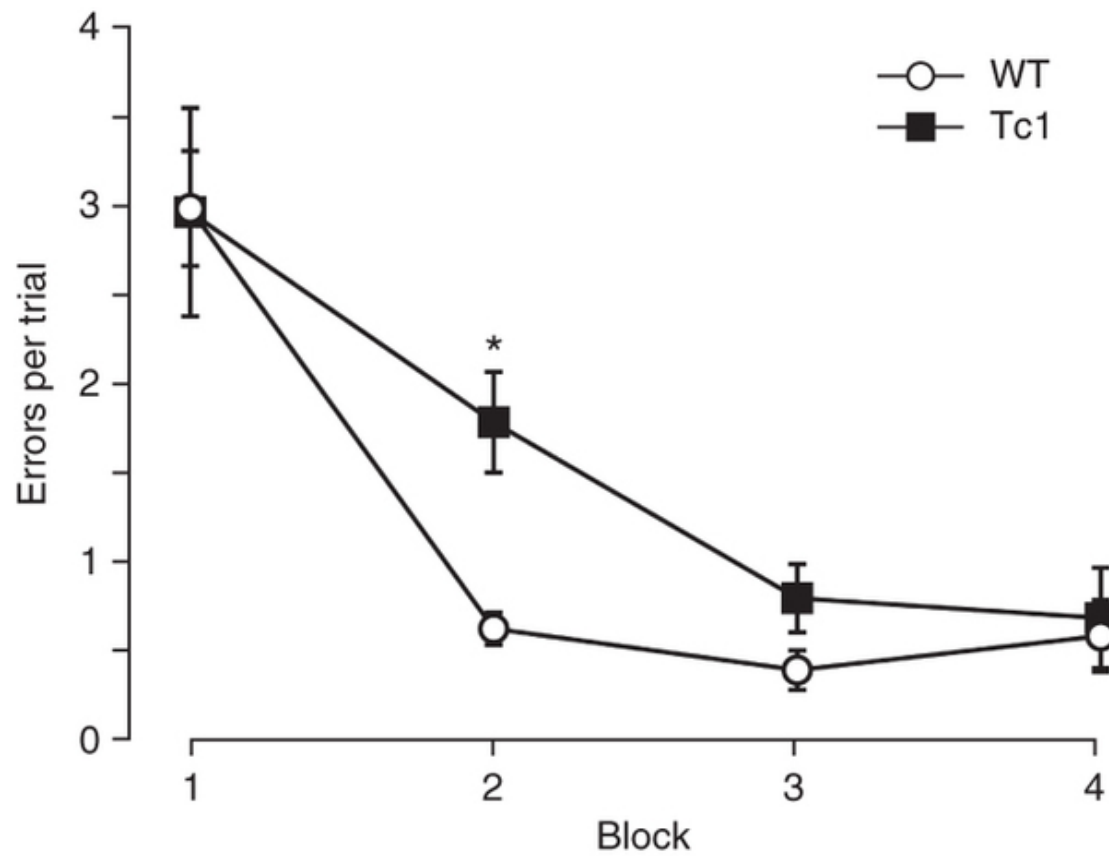
(a) Left, example 2-s traces from a representative wild-type (WT) CA3 pyramidal neuron illustrating mEPSCs recorded in control conditions and during application of 2 μ M DCG-IV; the fluorescence image (right) depicts the extent of thorny excrescences on this cell's apical dendrites (imaging settings as in [Fig. 4a,c](#)). (b) Equivalent example for a Tc1 CA3 pyramidal cell, exemplifying the reduced sensitivity of mEPSC frequency to DCG-IV application. (c) Group data showing average proportion (individual values in open circles, bars show mean \pm s.e.m.) of DCG-IV-sensitive mEPSCs in WT ($n = 10$ cells from 8 mice; $***P = 1.0 \times 10^{-4}$ compared to 100%, paired t -test) and Tc1 ($n = 14$ cells from 9 mice; $***P = 4.1 \times 10^{-4}$) CA3 pyramidal cells ($*P = 0.04$, non-equal-variance t -test). Square bracket highlights subgroup of DCG-IV-insensitive cells in Tc1 mice. (d) The proportion of DCG-IV-sensitive mEPSCs correlated positively with the area of thorny excrescences on a cell-by-cell basis (linear regression $P = 0.035$, Pearson's r^2 shown). (e) Example of electroporation labeling of MFs in CA3: a voltage pulse applied through a patch pipette electroporates several live MFs, loading them with Alexa Fluor 594; inset shows the fragment in dotted rectangle enlarged. Stars, white and yellow arrows depict two-dimensional projection views of typical MF giant, *en passant* and filopodial boutons, respectively (identified in three-dimensional stacks and counted in a blinded manner). (f) Average numbers of identifiable filopodial MF boutons (per one MF giant bouton) and *en passant* boutons (per 25 μ m of MF length) in the two genotypes (mean \pm s.e.m.; left to right, $n = 17, 17, 16, 16$ quasi-randomly sampled axonal fragments; WT-Tc1 group comparisons between filopodial and *en passant* samples give $P = 0.583$ and $P = 0.752$, respectively, rank sum test).

Figure 6: Impaired spatial information coding by CA3 and CA1 place cells in Tc1 mice.



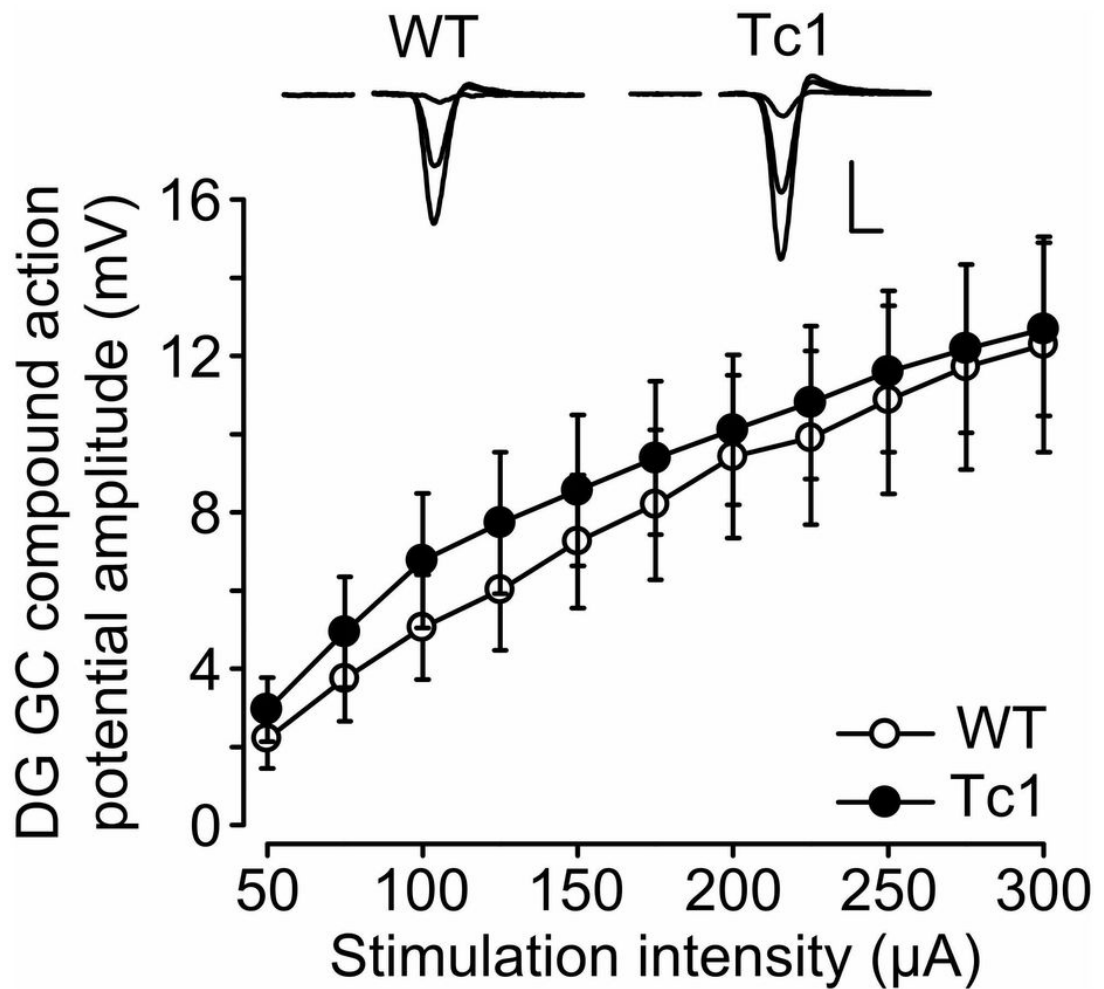
(a,b) Photomicrographs of Nissl-stained coronal brain sections illustrating tetrode tracts terminating in the CA3 and CA1 pyramidal cell layers (arrows) in wild-type (WT; a) and Tc1 (b) mice. Scale bars, 1 mm. (c,d) Scatter plots illustrating the waveform energies (Euclidean norm) of extracellular action potentials recorded on two channels of representative WT (c) and Tc1 (d) CA3 and CA1 tetrodes. Colors highlight clusters of action potentials discharged by individual neurons. Mean action potential waveforms on each tetrode channel (Ch1) are illustrated for the circled clusters above their respective scatter plot. Scale bars: WT 1 ms, 200 μ V (CA3), 50 μ V (CA1); Tc1 1 ms, 100 μ V (CA3), 250 μ V (CA1). (e) Trial-by-trial spatial firing for two representative WT CA3 (top) and CA1 (bottom) pyramidal cells; a single running direction is plotted for each cell, illustrated by arrows above raster plots. Track positions are plotted on the x axis, with each tick representing the firing position of an action potential. Trial-averaged positional firing rate histograms are plotted below. (f) Trial-by-trial raster plots and mean positional firing rates for two representative Tc1 CA3 and CA1 pyramidal cells, showing more spatially diffuse firing and reduced inter-trial firing stability. (g-i) Cumulative frequency plots illustrating the distributions of (g) place field sizes (CA3: $P = 0.039$, unpaired t -test; CA1: $P = 3.5 \times 10^{-4}$, rank sum test), (h) trial-by-trial rate stabilities (CA3: $P = 0.048$; CA1: $P = 0.042$, rank sum test) and (i) directionality indices (CA3: $P = 0.757$; CA1: $P = 0.001$, unpaired t -test) for WT and Tc1 CA3 and CA1 pyramidal neurons. Inset box plots show the median, first and third quartiles, and 99% confidence limits; inset line plots (for normally distributed data) show the mean and s.d.; n.s., $P > 0.05$; * $P < 0.05$; *** $P < 0.005$.

Figure 7: Tc1 mice show impaired spatial working memory on the radial arm maze.



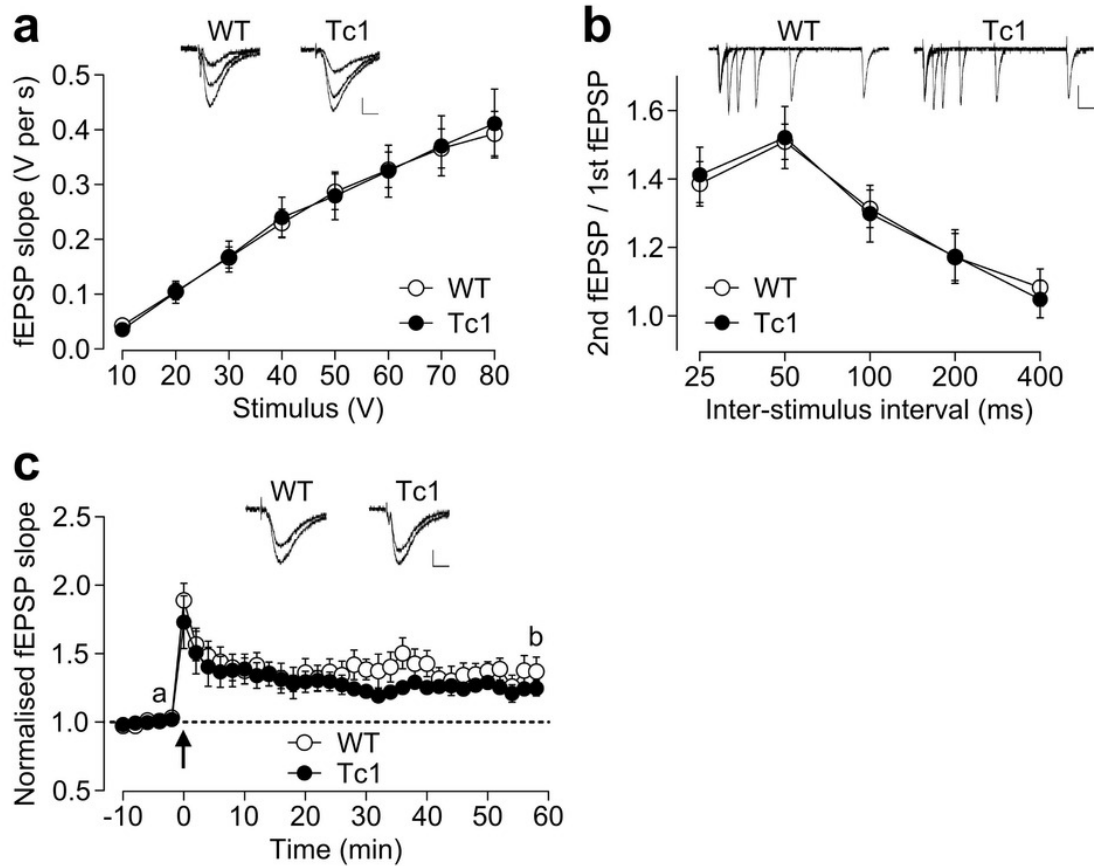
Mean \pm s.e.m. errors per trial for wild-type (WT; $n = 11$) and Tc1 ($n = 9$) mice on the spatial working memory, win-shift radial maze task. Blocks consist of 6 trials (1 trial per day); * $P = 0.004$, two-way ANOVA with *post hoc* test for simple main effects.

Supplementary Figure 1: Normal granule cell excitability in Tc1 mice.



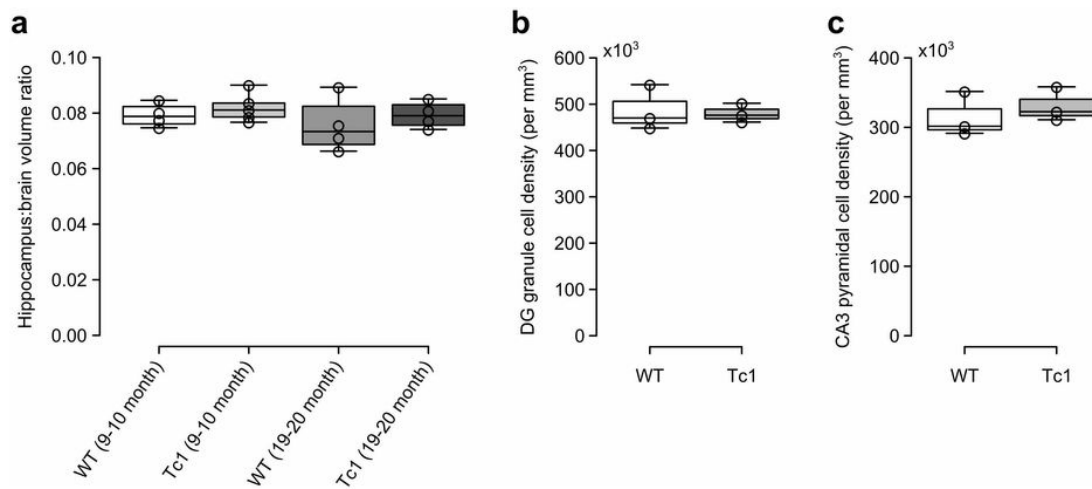
Pooled stimulus-response curves showing the mean \pm SEM amplitude of antidromically-evoked compound action potential recorded in the granule cell (GC) layer of dentate gyrus (DG) vs. the strength of stimulation applied to mossy fibers in area CA3. Data are pooled from slices prepared from 7 wild-type (WT) and 6 Tc1 mice. Inset traces show example responses at 50, 150 and 300 μ A stimulation. Scale bar: 1ms, 5mV. $P=0.70$, $F(1,11)=0.15$, two-way mixed ANOVA.

Supplementary Figure 2: Normal synaptic function in the Schaffer collateral pathway in Tc1 mice.



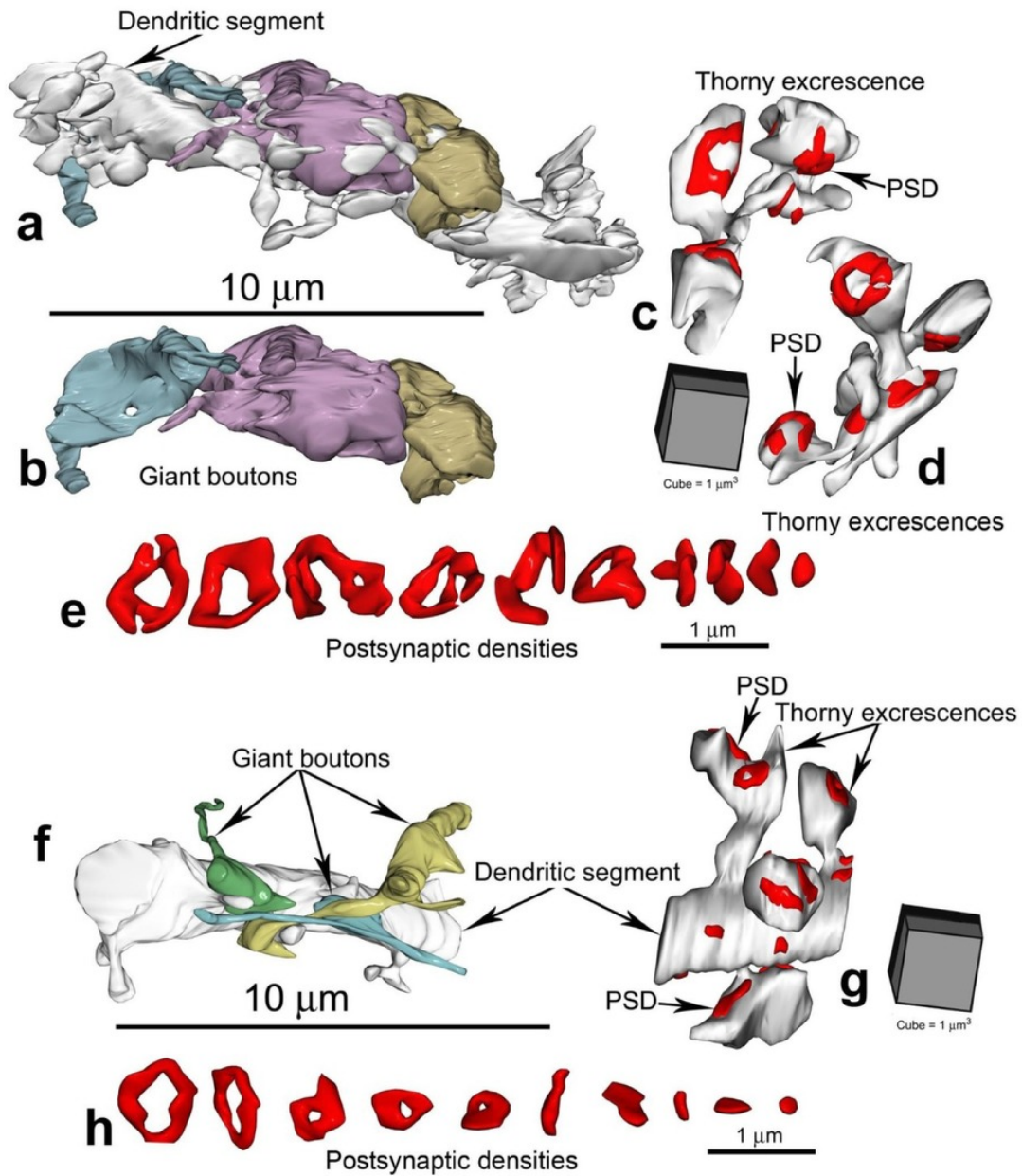
(a) Pooled CA3-CA1 stimulus-response curves for recordings made in hippocampal slices from wild-type (WT) and Tc1 mice (mean \pm SEM). Inset traces show overlaid example responses to 20, 40 and 80V stimulation for the two genotypes. (b) Pooled CA3-CA1 paired-pulse facilitation curves for paired stimuli delivered over inter-stimulus intervals from 25-400ms. Traces show example responses at each inter-stimulus interval. (c) Pooled data from CA3-CA1 LTP experiments in wild-type and Tc1 mice. Arrow denotes delivery of the conditioning stimulus (200ms, 100Hz repeated 3x at 1.5s intervals). Traces show example responses at times a and b. Scale bars: 5ms, 0.25mV.

Supplementary Figure 3: Normal hippocampal volumes and dentate granule cell and CA3 pyramidal cell densities in Tc1 mice.



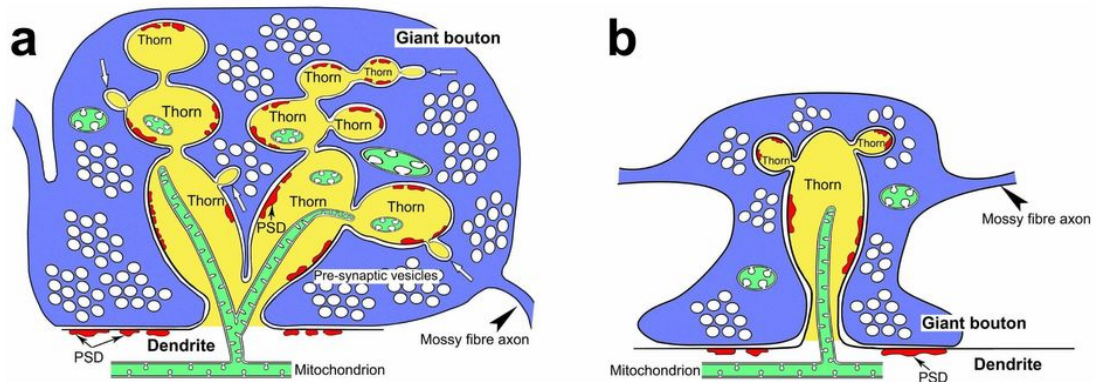
(a) Hippocampus:brain volume ratios in wild-type (WT) and Tc1 mice. For each box-plot, the center line illustrates the median and box limits indicate the 25th and 75th percentiles (determined using R software). Whiskers extend to the minimum and maximum values. Individual data points are plotted as open circles. n=4, 5, 4, 4 mice per sample respectively. (b) Dentate gyrus (DG) granule cell densities (per mm³) in wild-type (n=3) and Tc1 (n=3) mice. (c) Area CA3 pyramidal cell densities (per mm³) in wild-type (n=3) and Tc1 (n=3) mice.

Supplementary Figure 4: Three-dimensional reconstructions of CA3 dendritic segments, thorny excrescences and postsynaptic densities in wild-type and Tc1 mice.



Dendritic segments and associated presynaptic giant boutons from (a) wild-type and (f) Tc1 mice. Boutons are shown separately in (b) for the wild-type example. Typical examples of thorny excrescences with their postsynaptic densities (PSD) shown in red from (c-d) wild-type and (g) Tc1 mice. 10 representative PSDs from (e) wild-type and (h) Tc1 mice, showing reduced PSD volume in Tc1 animals.

Supplementary Figure 5: Schematic comparison of thorny excrescences in wild-type and Tc1 mice.



(a) Wild-type mice. (b) Tc1 mice. Prominent features in the Tc1 mice are: (1) retraction of thorns on thorny excrescences (yellow); (2) decrease in the volume of mossy fibre giant boutons (blue); (3) rearrangements of postsynaptic densities (PSD; red); (4) retraction of mitochondria from thorny excrescences (green). Note that dendritic spines in CA1 and dentate gyrus do not contain mitochondria.